Interannual-to-Multidecadal Responses of Antarctic Ice Shelf–Ocean Interaction and Coastal Water Masses during the Twentieth Century and the Early Twenty-First Century to Dynamic and Thermodynamic Forcing

KAZUYA KUSAHARA

Japan Agency for Marine-Earth Science and Technology, Yokohama, Kanagawa, Japan, and Antarctic Climate and Ecosystems Research Centre, University of Tasmania, Hobart, Tasmania, Australia

(Manuscript received 4 September 2019, in final form 8 March 2020)

ABSTRACT

Much attention has been paid to ocean–cryosphere interactions over the Southern Ocean. Basal melting of Antarctic ice shelves has been reported to be the primary ablation process for the Antarctic ice sheets. Warm waters on the continental shelf, such as Circumpolar Deep Water (CDW) and Antarctic Surface Water (AASW), play a critical role in active ice shelf basal melting. However, the temporal evolution and mechanisms of the basal melting and warm water intrusions throughout the twentieth century and the early twenty-first century have not been rigorously examined and are not fully understood. Here, we conduct a numerical experiment of an ocean–sea ice–ice shelf model forced with a century-long atmospheric reanalysis for the period 1900–2010. To begin with, we provide an assessment of the atmospheric conditions by comparing with available observation and show biases in warming and stronger westerly trends. Taking into account the limitation, we examine the interannual-to-multidecadal variability in the Antarctic ice shelf basal melting and the role of coastal water masses. A series of numerical experiments demonstrate that wind stress changes over the Southern Ocean drive enhanced poleward heat transport by stronger subpolar gyres and reduce coastal sea ice and cold-water formations, both of which result in an increased ocean heat flux into Antarctic ice shelf cavities. Furthermore, an increase of sea ice–free days leads to enhanced regional AASW contribution to the basal melting. This study demonstrates that changes in Antarctic coastal water masses are key metrics for better understanding of the ocean–cryosphere interaction over the Southern Ocean.

1. Introduction

An increasing number of in situ and satellite measurements in the second half of the twentieth century have uncovered changes in the Antarctic and Southern Ocean climate over the past few decades (Turner et al. 2009, 2014; Convey et al. 2009). The Antarctic and Southern Ocean climate consist of several physical components: Antarctic ice sheets/ice shelves, Antarctic sea ice, and the Southern Ocean. These subsystems interact with each other, as well as with the southern high-latitude atmosphere. Recent satellite analyses have shown that the Antarctic ice sheets have experienced accelerated ice discharge across the grounding line to the Southern Ocean (Rignot et al. 2008, 2011). The Antarctic ice shelves, floating parts of the ice sheets, have also shown profound thinning linked with the accelerated upstream ice flows in several sectors (Shepherd et al. 2010; Pritchard et al. 2012; Paolo et al. 2015) and frequent collapse events on the ice shelves at the Antarctic peninsula (Cook et al. 2005, 2016). In contrast to the shrinking of the ice sheets and ice shelves, the total Antarctic sea ice extent has displayed a modest increase since the late 1970s (Parkinson and Cavalieri 2012; Comiso et al. 2017; De Santis et al. 2017; Parkinson 2019), with considerable regional variability (Comiso et al. 2011; Stammerjohn et al. 2012; Holland 2014). The Southern Ocean has experienced decadal warming and freshening (Gille 2002; Sallée 2018). Significant warming trends have been identified in the north of Antarctic Circumpolar Current (Armour et al. 2016; Swart et al. 2018), on the continental shelf regions in the Pacific sector (Schmidtko et al. 2014), and in deep layers over the circumpolar Southern

Denotes content that is immediately available upon publication as open access.

Corresponding author: Kazuya Kusahara, kazuya.kusahara@gmail.com

DOI: 10.1175/JCLI-D-19-0659.1

© 2020 American Meteorological Society. For information regarding reuse of this content and general copyright information, consult the AMS Copyright Policy (www.ametsoc.org/PUBSReuseLicenses).

Ocean (Purkey and Johnson 2010). In and south of the Antarctic Circumpolar Currents, there is a cooling trend at the surface, which is consistent with the modest, increasing sea ice trend in recent decades (Fan et al. 2014). Freshening signals along Antarctic coastal margins appear to arise from the enhanced melting of Antarctic ice sheets/shelves (Jacobs and Giulivi 2010). For further details on the Southern Ocean warming and changes in Antarctic sea ice over recent decades, the reader is referred to the following review papers: Jones et al. (2016), Hobbs et al. (2016a), and Sallée (2018).

Changes in the cryosphere and ocean over the Southern Ocean are primarily driven by atmospheric circulation changes in the Southern Hemisphere. The southern annular mode (SAM) is one of the dominant atmospheric modes of the Southern Hemisphere and is characterized by its almost circumpolar structure (Thompson and Wallace 2000; Marshall 2003). The SAM itself represents fluctuations in the atmospheric mass between the high and middle latitudes (measured by the pressure difference), and the SAM index is a measure of the strength and location of the prevailing westerly winds over the Southern Ocean (Marshall 2003; Fogt et al. 2009). The positive phase of the SAM indicates higher pressure in the midlatitudes and lower pressure over the Antarctic continent and coastal regions with the local minimum in the Amundsen and Bellingshausen Seas. The SAM index has been reported to have shifted to a more positive phase in recent decades (Abram et al. 2014), indicating stronger circumpolar westerlies.

Alongside the increasing number of instrumental records in recent decades, numerical models for atmosphere, ocean, sea ice, and land surface processes have been extensively developed along with the development of powerful supercomputers. To fully simulate Earth's physical environments, climate models, which combine the numerical models for atmosphere, land, ocean, and sea ice components, have been actively developed at several climate research centers (Flato et al. 2013), and results from these climate models have been utilized not only for climate research but also for informing policies through the influential reports of the Intergovernmental Panel on Climate Change (IPCC). This combination of more detailed observations and numerical models has contributed to greatly improve our understanding of the Antarctic and Southern Ocean climate and its impact on the rest of the global environment.

However, in the current-generation climate models, ice–ocean interaction between Antarctic ice sheets/ice shelves and the Southern Ocean is ignored or simply parameterized with freshwater runoff from the Antarctic continent. The first ocean–sea ice–ice shelf model with a realistic topography for the Southern Ocean was presented by Beckmann et al. (1999) and they utilized it for understanding large-scale ocean circulation and water mass distribution in the Weddell Sea. Over the past two decades since the late 1990s, several ocean models with a thermodynamic ice shelf component have been developed to directly simulate the ice–ocean interaction (Dinniman et al. 2016; Asay-Davis et al. 2017). Using such models with the thermodynamic ice shelf component, many studies have demonstrated the importance of the ice–ocean interaction over the Southern Ocean and its effect on the ocean and sea ice conditions (e.g., Hellmer 2004; Kusahara and Hasumi 2014). Since the typical horizontal scale of the Antarctic ice shelves (except three major ice shelves: the Filchner–Ronne, Ross, and Amery Ice Shelves) ranges from a few kilometers to 100 km in the offshore direction, most ice shelf–ocean modeling studies used a regional modeling framework to resolve the smaller ice shelves in detail. With an increase in the available computing resources, several modeling studies have tried to include almost all of the ice shelves in a single model, such as circumpolar Southern Ocean or global ocean models (Timmermann et al. 2012; Kusahara and Hasumi 2013; Schodlok et al. 2016; Mathiot et al. 2017; Naughten et al. 2018). Using future projections by climate models as input, several ice shelf–ocean models produced predictions of how Antarctic ice shelves will respond to future climate changes (Hellmer et al. 2012; Timmermann and Hellmer 2013; Obase et al. 2017; Naughten et al. 2018).

Several studies have focused on the Antarctic ice–ocean interaction under present-day (i.e., the last few decades) and future conditions; however, no study has yet investigated the long-term evolution of the Southern Ocean ice–ocean interaction over the twentieth century. While the number of observations is limited in the beginning of the twentieth century, there exist some available observations and supporting evidence for the ocean and sea ice conditions in the Southern Ocean (Hobbs et al. 2016b; Bracegirdle et al. 2019). In other words, century-scale observational evidence, which consists of fragmented observations in the first half of the twentieth century and the more complete modern records, allows us to assess the model representation and performance. For example, an ocean–sea ice model study by Goosse et al. (2009) was successful in reproducing the Southern Ocean and Antarctic sea ice conditions over the twentieth century. Furthermore, long-term atmospheric reanalysis datasets are starting to become available. Although of course lack or scarcity of observations in high-latitude regions of the Southern Hemisphere in the presatellite era (i.e., before 1979) casts doubt about the accuracy of the representation of the atmospheric conditions, such atmospheric reanalysis

datasets provide physically consistent atmospheric surface boundary conditions. Therefore, if we can obtain the validity of the atmospheric conditions, the century-scale atmospheric dataset is useful to force ocean models.

In this study, we assess the representation of the atmospheric reanalysis fields and perform comparisons with available observations and reconstruction to obtain the limitations and some confidence in using the dataset as the model's forcing (section 3). Then, we conduct a hindcast simulation from 1900 to 2010, using a coupled circumpolar ocean–sea ice–ice shelf model driven by atmospheric surface forcing derived from a century-scale atmospheric reanalysis data to examine the long-term linear trend and interannual-to-decadal variability in basal melting of the Antarctic ice shelves and to coastal water masses (section 4a). In this study, we show sea ice and ocean model results mainly for validation purposes (appendix). Furthermore, from a series of numerical experiments, we examine the factors responsible for these ocean–cryosphere changes. The century-scale hindcast and numerical experiments presented in this study are complementary to several previous studies that focused on ice–ocean interactions under future climate conditions. Although we admit the limitation of using the century-scale atmospheric reanalysis dataset as the model forcing, the long-term experiments allow us to examine how the ocean and cryosphere over the Southern Ocean respond to the presumable atmospheric changes during the twentieth century and the early twenty-first century.

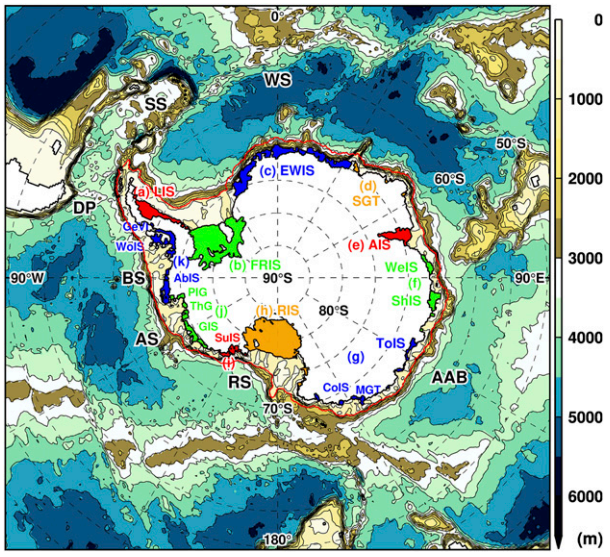

FIG. 1. Model bottom topography. Here, 11 ice shelves (labels a–k) are shown by different colors (red, green, blue, or orange). The red line shows the defined boundary between the coastal and deep ocean (the far side of 120-km distance from the Antarctic coastline/ice front or 1000-m depth contour). Major place names are shown: Drake Passage (DP), Scotia Sea (SS), Weddell Sea (WS), Australian–Antarctic Basin (AAB), Ross Sea (RS), Amundsen Sea (AS), and Bellingshausen Sea (BS). Major ice shelves/glaciers are shown in the same grouping colors: Larsen Ice Shelves (LIS), Filchner–Ronne Ice Shelf (FRIS), Eastern Weddell Ice Shelves (EWIS), Shirase Glacier Tongue (SGT), Amery Ice Shelf (AIS), West Ice Shelf (WeIS), Shackleton Ice Shelf (ShIS), Totten Ice Shelf (ToIS), Mertz Glacier Tongue (MGT), Cook Ice Shelf (CoIS), Ross Ice Shelf (RIS), Sulzberger Ice Shelf (SuIS), Getz Ice Shelf (GIS), Thwaites Glacier (ThG), Pine Island Glacier (PIG), Abbot Ice Shelf (AbIS), Wordie Ice Shelf (WoIS), and George VI Ice Shelf (GeVI).

2. Numerical model and experiments

a. An ocean–sea ice–ice shelf model

This study used the same coupled ocean–sea ice–ice shelf model as that used in Kusahara and Hasumi (2013, 2014). The model domain was the circumpolar Southern Ocean from 83.5° to 14.15°S (Fig. 1). The model horizontal resolution was set to $0.5° \times 0.5° \cos\varphi$ on the geographical longitude–latitude grid system. This configuration resulted in an isotropic grid system, with the horizontal resolution ranging from 6.4 km at the southernmost grid cells to 54 km at the northernmost grid cells (approximately 23-km resolution at 65°S for typical Antarctic coastal regions). Note that this intermediate horizontal resolution is not enough to reproduce ocean eddies but allows us to conduct century-long numerical experiments. The vertical coordinate system of the ocean model was a hybrid of σ and z coordinates; the σ coordinate was applied to the uppermost three levels between the free surface and 15 m, and the z coordinate was applied at depths below that. The vertical grid spacing in the z-coordinate region was 5 m (1 grid cell) just below the σ coordinate and 20 m (99 grid cells) in the depth range from 20 to 2000 m. Between 2000 and 5000 m, we used 75 levels at a spacing of 40 m and below that we used 10 levels at a spacing of 100 m. The maximum ocean depth in the model was set to 6000 m. It is noted that this vertical grid spacing is much finer than that in a typical z-coordinate model (up to a few hundred meters for a large-scale ocean model) and it was intended to well represent water mass exchange across the shelf break regions in the intermediate horizontal resolution model. The ice shelf component was only applied over the z-coordinate region. A partial step representation was adopted for both the bottom topography and the ice shelf draft to represent them optimally in the z-coordinate ocean model (Adcroft et al. 1997). The model bottom topography and ice shelf draft (Fig. 1) were derived from the RTopo-2 dataset (Schaffer et al. 2016).

The ocean model used isopycnal diffusion with the coefficient of $10.0\,m^2\,s^{-1}$, isopycnal layer thickness

diffusion with the coefficient of $3.0\,m^2\,s^{-1}$ (Gent et al. 1995), and a surface mixed layer scheme in the open ocean (Noh and Kim 1999). The background vertical diffusion and viscosity coefficients were set to 2.0×10^{-5} and $1.0 \times 10^{-4}\,m^2\,s^{-1}$, respectively. Horizontal eddy viscosity was a Laplacian form with the spatially varying coefficient to locally resolve the Munk layer. The bottom friction was parameterized by a simple quadratic law with a constant drag coefficient of 1.3×10^{-3}. A simple convective adjustment scheme was utilized to remove unstable stratification.

The sea ice component used one-layer thermodynamics (Bitz and Lipscomb 1999) and a two-category ice thickness representation (Hibler 1979). The prognostic equations for momentum, mass, and concentration were taken from Mellor and Kantha (1989). The internal ice stress was formulated by elastic–viscous–plastic rheology (Hunke and Dukowicz 1997) and the sea ice salinity in the model was fixed at 5 psu. High sea ice production areas (e.g., coastal polynyas) can also form on the downwind/downstream side of lines of small grounded icebergs, as well as along coastlines and ice fronts (Massom et al. 1998; Fraser et al. 2012; Nihashi and Ohshima 2015). To incorporate this unresolved blocking effect of sea ice advection by grounded icebergs in the model, we introduced lines of small grounded icebergs at several grid points by setting the sea ice velocity to zero (Kusahara et al. 2010). Note that oceanic flow was permitted in these grid cells. We placed these prescribed lines in the Cape Darnley, Mertz Glacier, and Amundsen Sea polynya regions (Nihashi and Ohshima 2015). As a first-order approximation, we ignored spatiotemporal variability in the grounded icebergs' positions throughout the model experiments. The treatment can be partially justified by the facts that icebergs stochastically ground at these shallow coastal regions and that the bottom topography is invariant on our focal time scale.

In the ice shelf component, we assumed a steady shape in the horizontal and vertical directions. The freshwater flux at the base of ice shelves was calculated with a three-equation scheme, based on a pressure-dependent freezing point equation and the conservation equations for heat and salinity (Hellmer and Olbers 1989; Holland and Jenkins 1999). Since this model was not eddy resolving and did not incorporate tidal forcing, we used the velocity-independent coefficients for the thermal and salinity exchange velocities (i.e., $\gamma_t = 1.0 \times 10^{-4}$ and $\gamma_s = 5.05 \times 10^{-7}$; Hellmer and Olbers 1989). It should be noted that most of the recent ice shelf–ocean modeling studies have used the velocity-dependent coefficients. Since velocity magnitudes under the ice shelves strongly depend on the horizontal and vertical grid resolutions, we preferred using the velocity-independent version in this study. For simplicity, we ignored heat flux from the ocean into ice shelf (in other words, the ice shelf is a perfect insulator). The modeled meltwater flux and the associated heat flux were distributed to a 30-m mixed layer (i.e., 1.5 vertical grids) under the ice shelf–ocean interface.

The initial values for the ocean temperature and salinity fields were derived from the Polar Science Center Hydrographic Climatology (Steele et al. 2001), and the ocean velocity was set to zero over the model domain. Water properties in the ice shelf cavities were extrapolated from those in the nearest open ocean. In the northernmost six grid cells (north of 17.5°S), the water properties of the temperature and salinity were restored to the monthly climatology throughout the water column with a 10-day damping time scale. Furthermore, sea surface salinity in offshore regions (see red line in Fig. 1 for the boundary) was also restored to the monthly mean climatology with a 10-day damping time scale to suppress unrealistic deep convection in some regions. The atmospheric surface boundary conditions for the model are wind stresses, wind speed, surface air temperature, specific humidity, downwelling longwave radiation, downwelling shortwave radiation, and water flux (precipitation/snow). We calculated these daily surface boundary conditions from the ERA-20C dataset (Poli et al. 2016) for the period 1900–2010, using the bulk formula of Kara et al. (2000). Note that in the bulk formula wind speed is used for calculating sensible and latent heat fluxes. There is a known cold bias in ERA20 with a magnitude of about 1°C, and therefore we applied a +1°C correction to the surface air temperature. The numerical model was first integrated for 100 years using the atmospheric conditions in the early twentieth century (the 1900-yr conditions for the first and last 10 years and four cycles of 20-yr interannually varying conditions from 1901 to 1920) to obtain a quasi-steady state in the ocean and sea ice fields for the year 1900. After the spinup integration, we carried out a hindcast simulation with interannually varying surface boundary conditions for the period 1900–2010 (the CTRL case). To assess drift and inherent variability in the model, an experiment repeatedly forced with the 1900-yr conditions for the same period was also conducted (the CNST case).

b. *Numerical experiments to identify roles of dynamic and thermodynamic surface forcing*

We performed two numerical experiments (the DYN and THD cases) in which different atmospheric surface boundary conditions were fixed at the 1900-yr conditions to separate the effects of dynamic (wind stress) and thermodynamic surface conditions on the modeled

fields in the CTRL case. In the DYN case, only wind stresses in the surface boundary conditions varied interannually (as in the CTRL case), and the other boundary conditions were fixed at the 1900-yr conditions. Similarly, in the THD case, only the thermodynamic boundary conditions varied interannually. We conducted a 110-yr integration from 1901 to 2010 for each experiment. Comparing the results from the three experiments allows us to examine the relative roles of wind stress and thermodynamic surface forcing on the modeled fields. Note that in these experiments dynamic and thermodynamic conditions are not physically consistent with each other due to the different years.

3. Comparisons of the reanalysis atmospheric fields with available observations

In this section, we show the spatial patterns of the annual mean, linear trend, and standard deviation of key atmospheric variables [mean sea level pressure (MSLP), 10-m wind, and 2-m temperature] in the ERA20C reanalysis for the period 1900–2010 (Fig. 2). The standard deviation (right panels in Fig. 2) was calculated after removing the linear trend components. The representation of the atmospheric fields directly links to the reliability of the results from the ocean–sea ice–ice shelf model forced with the atmospheric surface boundary conditions. Therefore, we compare the atmospheric reanalysis fields with available observation-based evidence (air temperature observations at Antarctic stations from the READER database (Turner et al. 2004, 2019) and three SAM indices) to provide an assessment of the atmospheric conditions in the high-latitude Southern Hemisphere. Figure 3 is scatter diagrams of the temperature trend and variability and SAM trend for quantitative comparison.

In the long-term mean MSLP field (Fig. 2a), there is a circumpolar pattern of low pressure at high southern latitudes and high pressure at lower latitudes with three regional minimums, the centers of which are at around 30°E, 90°E, and 90°W. Consistent with the pressure pattern, a prevailing westerly wind exists over the Southern Ocean (Fig. 2d). Along the Antarctic coastal margins (regions within approximately 500 km of the Antarctic coastline), a prevailing easterly wind regime is also identified. In the annual-mean air temperature field (Fig. 2g), circumpolar strong temperature gradients are present between the Antarctic coastal margins and midlatitudes, with a magnitude of more than 20°C.

The MSLP has a strong negative trend south of 55°S at all longitudes (Fig. 2b), leading to a circumpolar stronger westerly wind (a positive trend in the eastward wind) over most of the Southern Ocean (Fig. 2e). This circumpolar pattern clearly represents the positive shift in the SAM (Abram et al. 2014). ERA20C's SAM index, defined by the difference of the normalized zonal mean MSLP at 40° and 65°S (Gong and Wang 1999), is shown with red in Fig. 4, with the observation-based SAM indices (Marshall 2003; Fogt et al. 2009; Abram et al. 2014). All the SAM indices demonstrate positive trends during the analyzed periods in the twentieth century, although the magnitudes of the linear trend and temporal variability are different among them. Particularly, pronounced differences are identified in the period before the 1940s. On the other hand, after the 1940s, all the indices vary in the range from −2 to +1 with their positive trends [but with larger temporal variability in the index from Abram et al. (2014)]. Although, of course, the magnitude of the linear trends depends on the length of the analysis period, ERA20C's SAM trend is overestimated (Fig. 3c). ERA20C's SAM trend for the period 1905–2004 is approximately 5 times larger than Fogt's trend. The overestimation of ERA20C's SAM trend mainly comes from the vast difference before 1940 (e.g., the large negative phase in ERA20C). The trend comparison without the period before the 1940s alleviates the trend biases in ERA20C's SAM index: ERA20C's SAM trend is comparable to Abram's trend and is nearly double of Marshall's and Fogt's trends (Fig. 3c). These analyses suggest that ERA20C has a relatively good representation of the large-scale atmospheric circulation changes in the high-latitude Southern Hemisphere in the period after the 1940s.

Looking at the air temperature trend (Fig. 2h), there are warming trends (approximately 2°C century^{-1}) along the Antarctic coastal margins, except over the Ross Sea where the air temperature shows a negative trend. A pronounced warming trend is represented in the Bellingshausen–Antarctic Peninsula region in the ERA20C dataset. This pattern is consistent with the trend pattern derived from the synthesized air temperate dataset for the period 1958–2002 (Chapman and Walsh 2007). Furthermore, we utilized the READER database (Turner et al. 2004, 2019) to assess the regional ERA20C's temperature trend at Antarctic stations (15 for coastal/island stations and 2 for inland stations; see Fig. 2g for the locations). Although it should be noted that the lengths of the station record depend on the location, the temperature trend in the ERA20C dataset for the period 1900–2010 does not conflict with the observed trends in recent decades (Fig. 3a). ERA20C's temperature trend at eight stations (1, 5, 8, 10, 11, 13, 14, and 15) are within the range of 50%–200% of the observation, those at five stations (3, 4, 7, 9, and 12) where the magnitude of the observed temperature trend is small are more than double, and

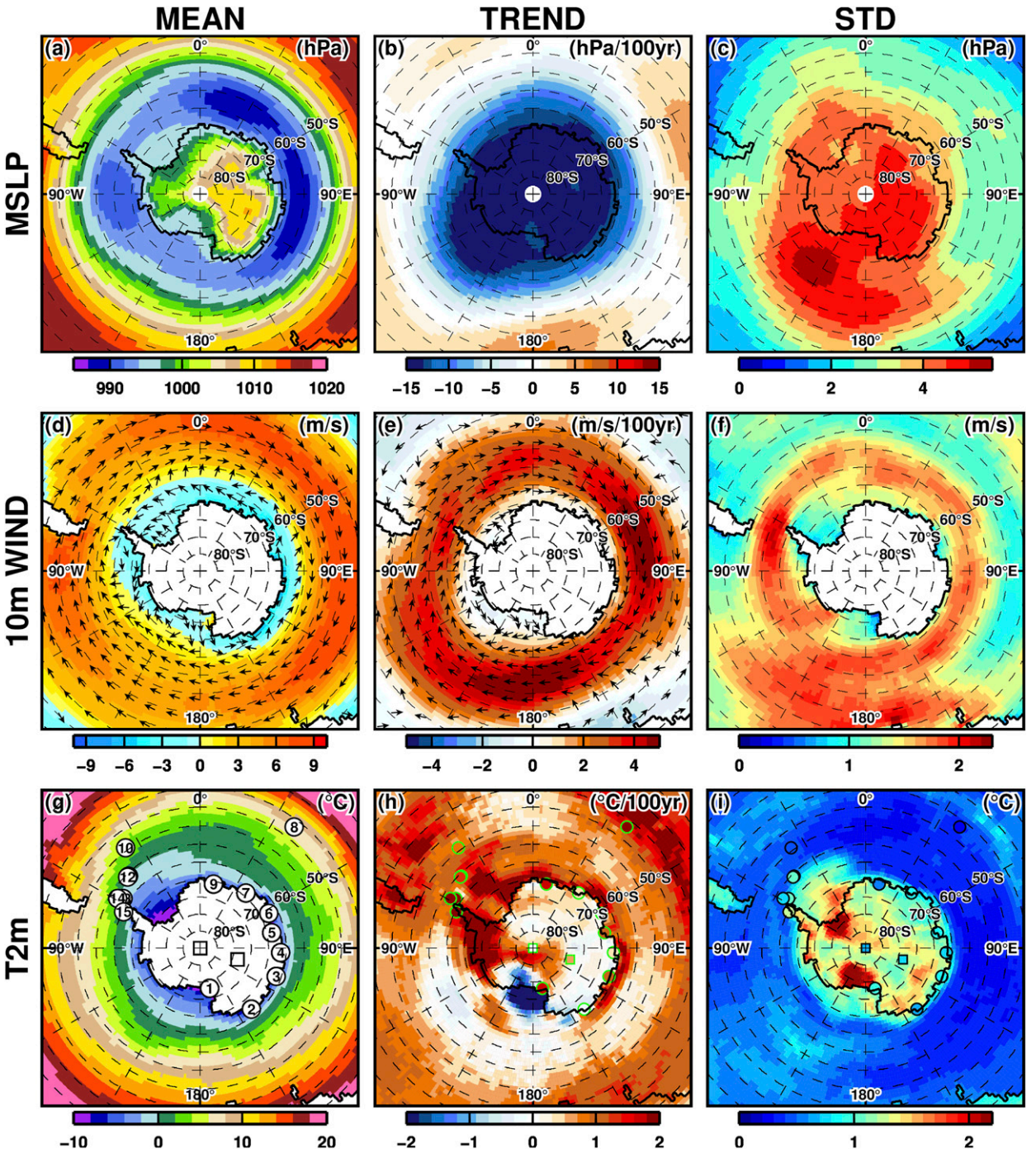

FIG. 2. Maps of mean, linear trend, and standard deviation in (a)–(c) mean sea level pressure, (d)–(f) 10-m wind, and (g)–(i) 2-m temperature for the period 1900–2010. Colors in (d)–(f) represent the zonal wind component. In (h) and (i), observed temperature trends and standard deviation at 15 coastal/island stations [Scott Base (77.9°S, 166.7°E), Dumont Durville (66.7°S, 140.0°E), Casey (66.3°S, 110.5°E), Mirny (66.5°S, 93.0°E), Davis (68.6°S, 78.0°E), Mawson (67.6°S, 62.9°E), Syowa (69.0°S, 39.6°E), Marion (46.8°S, 37.8°E), Novolazarevskaya (70.8°S, 11.8°E), Grytviken (54.3°S, 36.5°W), Orcadas (60.7°S, 44.7°W), Signy (60.7°S, 45.6°W), Esperanza (63.4°S, 57.0°W), Bellingshausen (62.2°S, 58.9°W), and Faraday (65.4°S, 64.4°W)] and two inland stations [Amundsen Scott (90.0°S, 0.0°) and Vostok (78.5°S, 106.9°E)] are shown by circles and squares, respectively. The lengths of the observed annual mean temperature at the stations are longer than 40 years. The coastal/island stations are labeled with numbers 1–15 in (g).

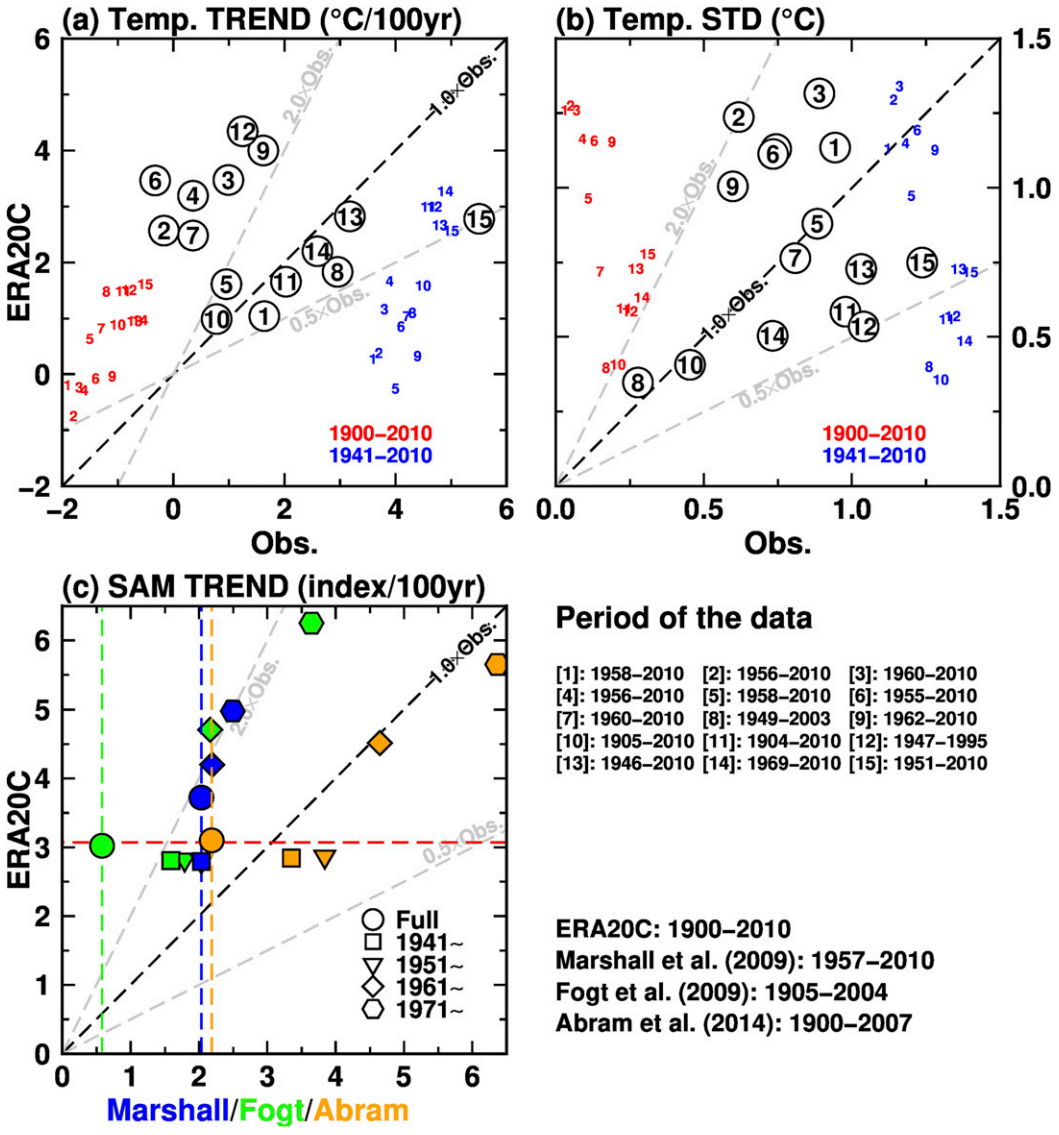

FIG. 3. Scatter diagrams of (a) air temperature trend, (b) standard deviation, and (c) SAM index trend. The black dashed line in each panel indicates 100% of the observed estimate, and two gray dashed lines indicate 50% and 200% of the observed value. In (a) and (b), the values (trend and standard deviation) estimated with different periods (1900–2010 and 1941–2010) are shown in red and blue numbers with appropriate horizontal offsets. In (c), colored dashed lines indicate the linear trend for the full length in each data. Plots with marks show trends in the same periods between ERA20C and observation-based estimates. Squares, inverse triangles, diamonds, and hexagons show the trends with a different starting year.

those at two stations (2 and 6) show the wrong sign. Note that the magnitude of the air temperature trend is sensitive to the analysis period (see red and blue numbers in Fig. 3a). The cooling trend in the Ross Sea in the ERA20C dataset is not validated with the observation (Fig. 2h). The observed temperature trend at Scott Base (a coastal station in the Ross Sea), next to the cooling trend region, is positive (+1.63°C century^{-1} for the period 1958–2010). The regional trend is also captured in the ERA20C dataset, but with a smaller magnitude (Fig. 3a).

Time series of the air temperature anomaly (with respect to the 1981–2000 mean) in the regions south of 60°S and over the Southern Ocean are shown in Fig. 5 to examine the temporal variability in the ERA20C dataset. ERA20C's temperature trends for the periods 1900–2010 and 1958–2002 are 0.55° and 2.68°C century^{-1}, respectively. The later period is the same analysis

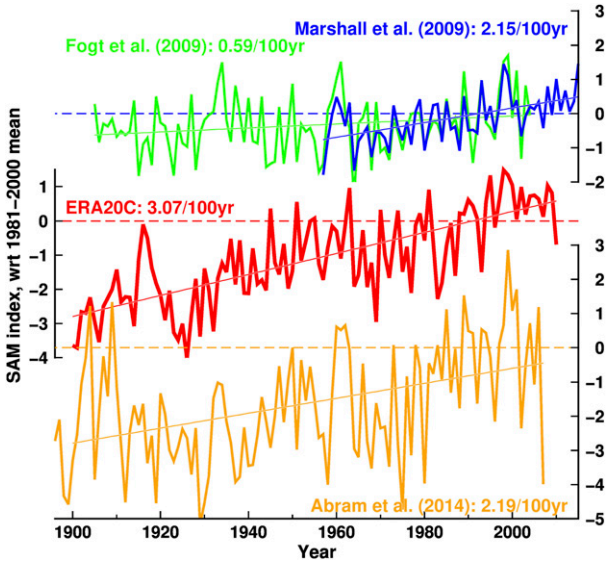

FIG. 4. Time series of SAM index. Blue, green, and orange curves represent the SAM reconstructions by Marshall (2003), Fogt et al. (2009), and Abram et al. (2014), respectively. Red is the SAM index in ERA20C with the calculation method of Gong and Wang (1999), the difference of the normalized zonal mean sea level pressure at 40° and 65°S. All the SAM indices are shown as the anomaly with respect to the 1981–2000 mean. The dashed lines show the zero line for the indices. The straight solid line in each curve indicates the linear trend in the available periods (blue for 1957–2010 and green for 1905–2004) or 1900–2010 (red and orange) and the magnitudes of the trend are shown in the same color.

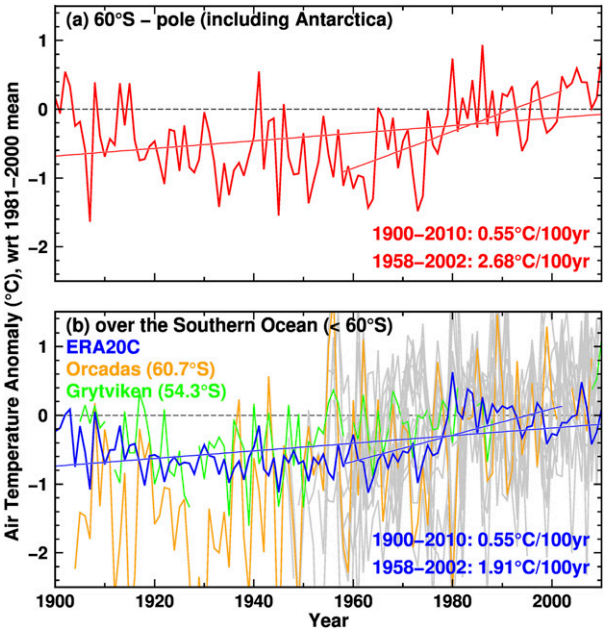

FIG. 5. Time series of air temperature anomalies with respect to the 1981–2000 mean in ERA20C: (a) average in the region south of 60°S and (b) average over the ocean south of 60°S. The straight lines represent the linear trends for the periods 1900–2010 and 1958–2002. The period of 1958–2002 is the same analysis period in Chapman and Walsh (2007). In (b), time series of the observed air temperature anomaly at 13 coastal stations (gray), Orcadas (orange; 1904–2010), and Grytviken (green; 1905–2010) are shown (refer to Fig. 2g and the captions for the locations of the stations). Some station data have intermittent gaps.

period of Chapman and Walsh (2007) and their estimate for the temperature trend was 0.82°C century^{-1}, suggesting that the ERA20C overestimates the positive trend in the period by a factor of 3. The air temperature trends over the Southern Ocean for the periods are similar to or lower than those that include the Antarctic continent. We compare the temporal variability over the Southern Ocean in the ERA20C dataset with available observed air temperatures at the Antarctic coastal stations and two islands (see Fig. 2g for the locations). The observed records at Orcadas and Grytviken provide the longest time series to assess the air temperature throughout the twentieth century. Comparison of ERA20C's temperature over the Southern Ocean with the observations demonstrates that the air temperature over the Southern Ocean in the reanalysis seems to be consistent with the observed temperature variability after the 1940s, whereas before 1940 it is difficult to obtain conclusive validation with the two time series that diverge from each other.

In the standard deviation in the MSLP field (Fig. 2c), extensive regions of high variability are identified south of 55°S in the Atlantic and Indian sectors and south of 45°S in the Pacific sector. The local maximum in the variability is located at around 135°W and 65°S. The westerly wind has large fluctuations in the latitude band from 50° to 65°S (Fig. 2f). High variability in the wind extends toward the midlatitude areas in the Ross and the Amundsen Sea sectors (from 150°E to 120°W). Considerable variability in air temperature is confined to the Antarctic coastal margins (Fig. 2i). The large variability in the coastal regions and over the Southern Ocean is reasonably represented in the reanalysis dataset (Fig. 3b): the standard deviation at all the stations is within a range of 50%–200% of the observed variability.

4. Antarctic ice shelf basal melting and coastal water masses flowing into the ice shelf cavities

In section 4a, we show the climatological mean (with a comparison with the satellite-based estimates), the linear trends, and interannual-to-decadal variability of basal melting at all of the Antarctic ice shelves in the

CTRL case, and analyze the Antarctic coastal water masses flowing into the ice shelf cavities to identify the heat source for the melting. In section 4b, we examine the factors responsible for the linear trends and interannual-to-decadal variability in the ice shelf basal melting and the associated coastal water masses flowing into the cavities. A comparison of the results from the three numerical experiments (CTRL, DYN, and THD cases) allows us to estimate the relative roles of dynamic and thermodynamic surface forcing on the system. Although we focus on the ice shelf basal melting and coastal water masses in this section, we show in the appendix the model performance in the sea ice and ocean fields, which link with the coastal water masses formation.

a. CTRL case

This subsection details the modeled basal melting at Antarctic ice shelves and coastal water masses flowing into the ice shelf cavities. For convenience, we grouped the Antarctic ice shelves into 11 regions (see labels a–k in Fig. 1 for the ice shelf groups) and examine time series of the total and regional basal melt rate (Fig. 6). The total basal melting from all of the Antarctic ice shelves increases gradually from about 700 Gt yr^{-1} in the early 1900s to over 1100 Gt yr^{-1} in the 2000s (Fig. 6), corresponding to about a 50% increase. Since the atmospheric conditions before the 1940s were not fully assessed with the observational evidence (as shown in section 3), we henceforth calculate long-term linear trends for two periods (1900–2010 and 1941–2010). The substantially smaller magnitudes of the linear trends for the total basal melting in the CNST case (small negative trends) indicate that the linear trends in the CTRL case are meaningful in this model framework, not model drifts. All of the ice shelf groups show increasing basal melt trends over the two periods (Fig. 6). Along with the positive linear trends, there exists sizeable interannual-to-decadal variability, which is larger than the internal variability in the CNST case.

Here, we compare the present-day ice shelf basal melting amount in the CTRL case with the recent satellite-based estimates (Rignot et al. 2013; Depoorter et al. 2013). The observational estimates from Rignot et al. (2013) and Depoorter et al. (2013) are 1325 and 1193 Gt yr^{-1}, respectively, for their surveyed areas (their estimates are scaled up to 1500 and 1454 Gt yr^{-1} to take account contribution from the unsurveyed areas). We use their estimates as representative values of the observed basal melting in recent decades. The mean total melting amount in the CTRL case for the period 1981–2010 is 1035 Gt yr^{-1} and it is smaller than the observations. It should be noted that the magnitude of the basal melting in a numerical model depends on the treatments of ice shelf–ocean interaction, such as the parameterization, the coefficients, and grid sizes (Gwyther et al. 2020).

Figure 7 shows a regional comparison of ice shelf basal melting between the model and observations. The regional observational estimates were calculated from Table 1 in Rignot et al. (2013) and supplemental Table 1 in Depoorter et al. (2013). Except for the ice shelf groups C (EWIS) and J (GIS/ThG) (all expansions of ice shelf groups are provided in Fig. 1; group names are hereafter set with capital letters), the regional basal melting amounts in the CTRL case are within a range from 1/3 to 3 times the observational estimates, showing a reasonable representation of the basal melting in the intermediate horizontal resolution model. In the ice shelf group C (EWIS), the modeled basal melting is more than 3 times larger than the observations, whereas in ice shelf group J (GIS/ThG) the model profoundly underestimates the basal melting. These model biases may come from the insufficient model resolution, the associated processes, and/or inadequate surface forcing. It is known that some coarse /intermediate horizontal resolution models struggle to reproduce active basal melting in the Amundsen Sea region due to weak intrusion of warm water from continental shelf break and active cold water formation linked with stronger sea ice formation (Timmermann et al. 2012; Timmermann and Hellmer 2013; Nakayama et al. 2014). As we will show later, the model in this study underestimates warm water intrusions into the ice shelf cavities in the Amundsen and Bellingshausen Seas. Ice shelves in the eastern Weddell Sea region (i.e., the ice shelf group C) overhang continental shelves, and therefore the intermediate horizontal resolution model might exaggerate warm water intrusions oriented from offshore into the ice shelf cavities, resulting in the regional overestimation of the basal melting.

To classify Antarctic coastal water masses, we used the potential temperature and salinity to define six water masses (Table 1 and the *T*–*S* diagram in Fig. 8): HSSW, LSSW, MSW, MCDW, AASW, and ISW (the water mass abbreviations are explained just below). It should be noted that the water mass definitions used in this study are slightly unconventional (in terms of ignoring the density) but the simple definitions are convenient to roughly capture the amount of heat for basal melting and the types of inflowing water. The first five water masses are the heat source for the basal melting of the Antarctic ice shelves, while Ice Shelf Water (ISW) is a product of ice shelf–ocean interaction. Jacobs et al. (1992) introduced three modes for Antarctic ice shelf basal melting. The first mode is linked to cold Shelf Water (SW) formation in winter. When sea ice is formed, brine

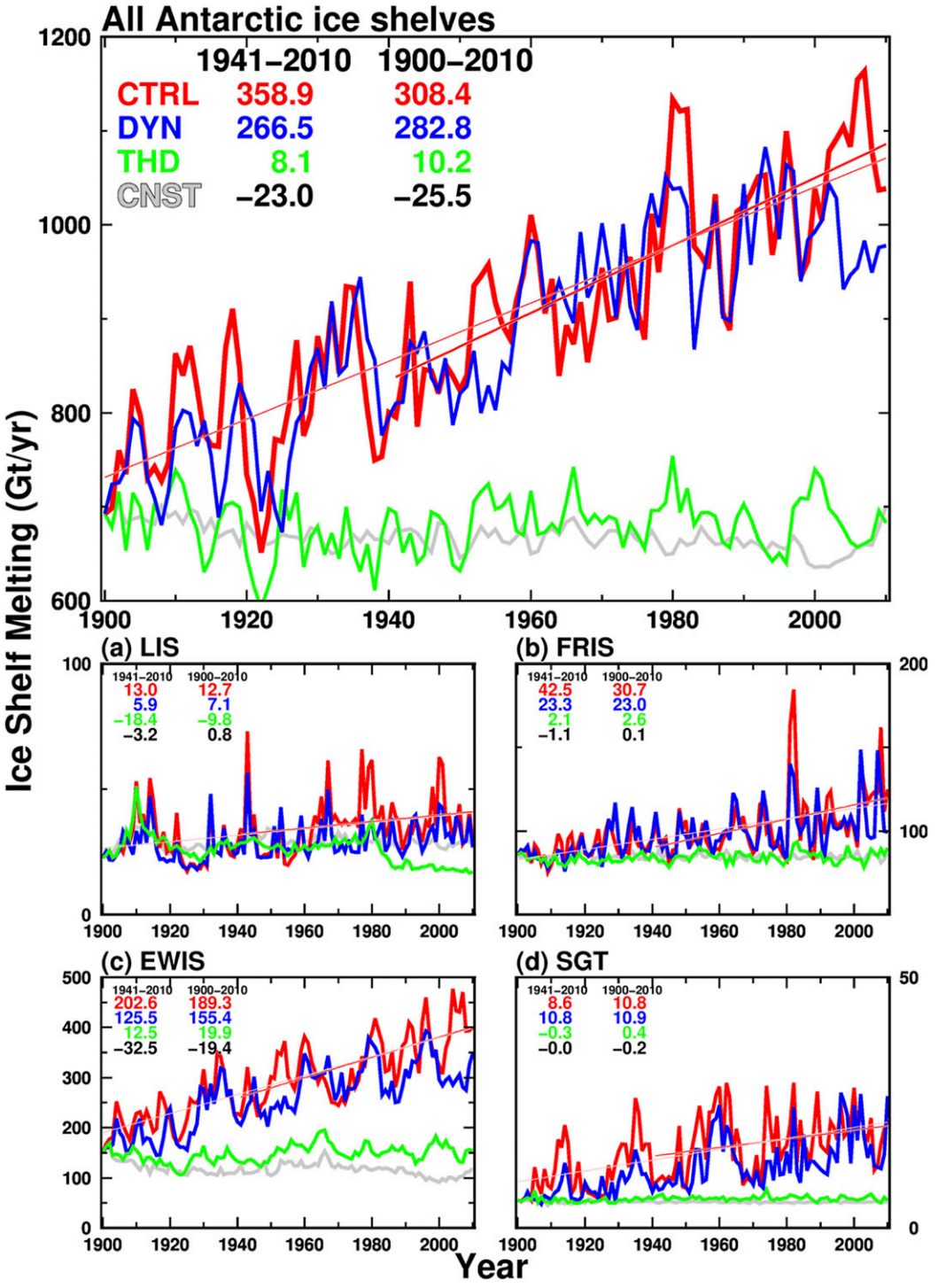

FIG. 6. Time series of the basal melting amount of Antarctic ice shelves. (top) The total melting amount from all Antarctic ice shelves and (a)–(k) the melting amount from the regional ice shelves. Red, blue, green, and gray curves are results from the CTRL, DYN, THD, and CNST cases, respectively. The thin and thick red straight lines represent the linear trends in the CTRL case for the periods 1900–2010 and 1941–2010, respectively. The magnitudes of the linear trends in the experiments for the two periods are shown in the upper left side of each panel.

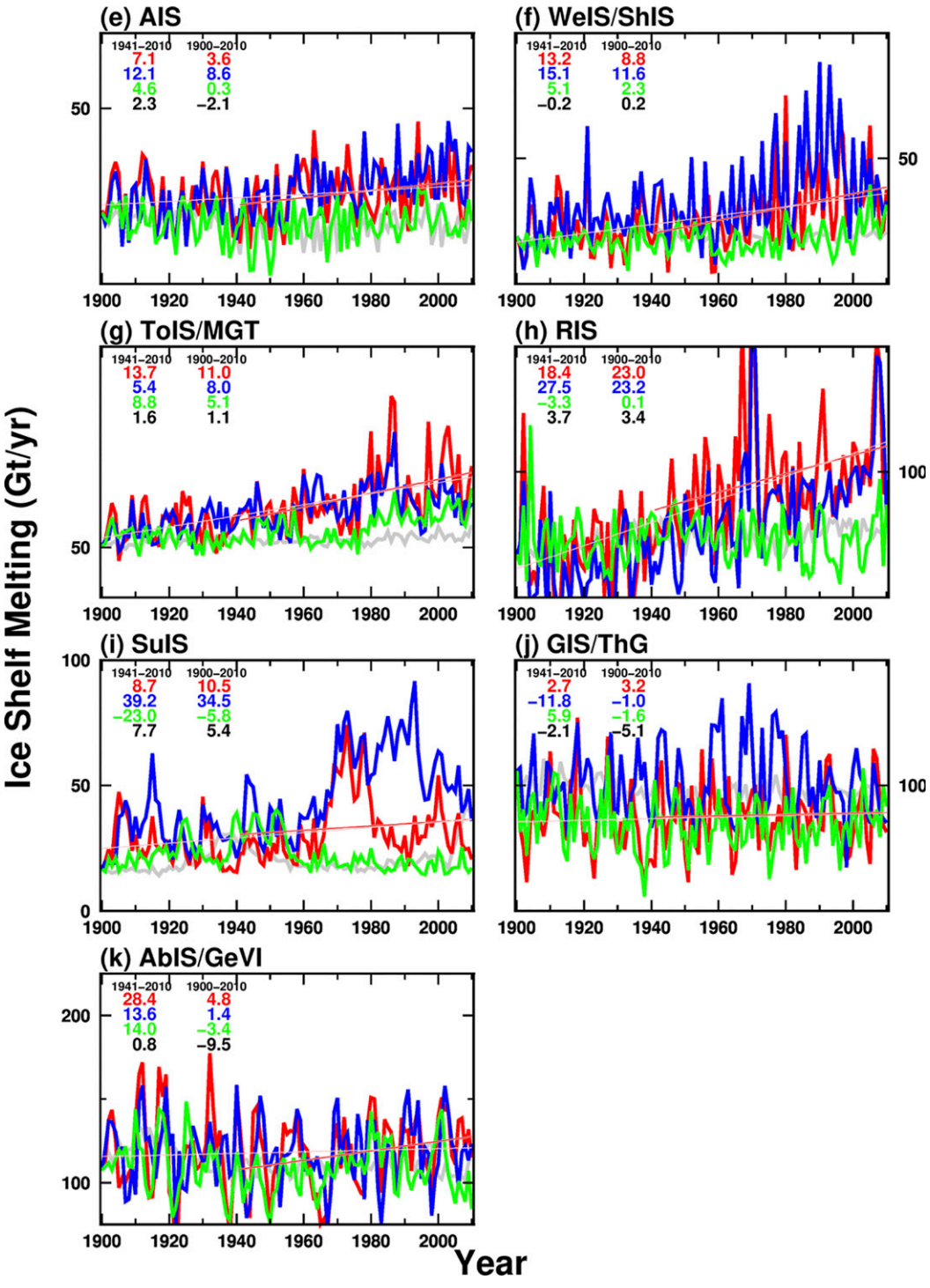

FIG. 6. (*Continued*)

water (which has surface freezing temperature and higher salinity than ambient coastal waters) is rejected (Morales Maqueda et al. 2004). SW is a product of a mixture of the brine and ambient waters, and thus this water mass is characterized by near-surface freezing temperature. We defined two SWs based on salinity: High Salinity Shelf Water (HSSW) and Low Salinity Shelf Water (LSSW). Since the freezing temperature of seawater

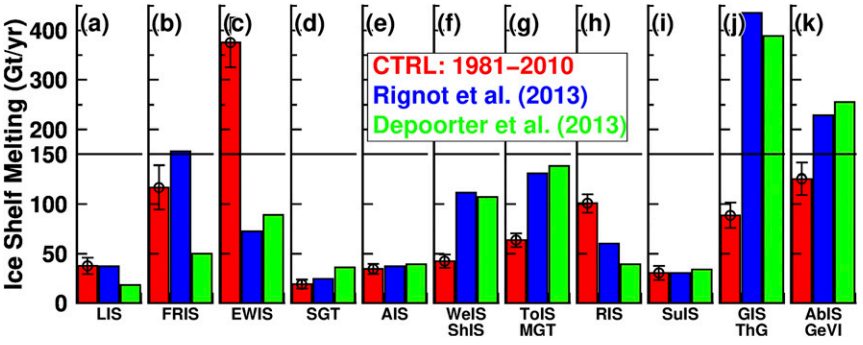

FIG. 7. Comparison of the modeled basal melting amount in the CTRL case (red) with the two observation-based estimates [blue: Rignot et al. (2013) and green: Depoorter et al. (2013)]. The modeled melting amount is the average over the period 1981–2010, and error bars show the standard deviation for the interannual variability. Different vertical scales are used below and above 150 Gt yr^{-1}.

strongly depends on depth and pressure, these water masses, even with near-freezing temperatures, can be a heat source for ice shelf melting (in particular ice shelves that have deep drafts). The second mode is related to an intrusion of warm and saline Circumpolar Deep Water (CDW), which is part of the Antarctic Circumpolar Current. Through topographic gaps at shelf breaks (i.e., troughs and sills), part of the CDW intrudes onto continental shelf regions and is modified by mixing with coastal waters, forming modified CDW (MCDW). A mixture of MCDW and SW (particularly HSSW) leads to modified SW (MSW). The temperatures of MCDW and MSW are warmer than those of SWs, and thus these water masses can cause active basal melting. The third mode is associated with Antarctic Surface Water (AASW). This water is formed by sea ice melting and thus has low salinities. In summer, AASW can be warmed by solar radiation and surface heating. Warm AASW is transported to ice shelf cavities by the tides and wind-driven seasonal coastal currents, resulting in active ice front melting.

Ocean heat flux across the ice fronts is the heat source for basal melting of Antarctic ice shelves, and thus we examine in detail the coastal water masses flowing into each ice shelf cavity, using plots of the percentage of water masses flowing into the cavities (Fig. 8) and linear trends (Figs. 9 and 10). In the trend analysis, linear trends in the mean temperature of the total inflow, inflow transports of the water masses, and coastal sea ice production in neighboring areas (within 120 km from the Antarctic coastline or ice shelf fronts) are shown to identify the factors responsible for basal melting at each ice shelf. From the plots of the time evolution of the coastal water masses flowing into the cavities (Fig. 8), it can be seen that the inflow patterns differ greatly from one ice shelf to another. Looking at the trends for all of the Antarctic ice shelves in the CTRL case (red bars in Figs. 9a–h), the basal melt rate and the mean temperature show significant positive trends, indicating that enhanced heat flux across the ice fronts leads to higher basal melting. Again, we show the trend in the CNST case to verify that the trends in the experiments are not model drifts. Decomposing the enhanced heat flux into water mass contributions, increased transports of MCDW, MSW, and AASW and a decrease in the transport of cold waters (the sum of HSSW and LSSW) contribute to the positive trend in the mean temperature and basal melting. The decreased transport of HSSW and LSSW is consistent with the reduction in sea ice production along Antarctic coastal margins (Fig. A5b). The increased transport of the warm waters is larger than the decreased transport of the cold waters, and thus the total transport into the Antarctic ice shelf cavities (Fig. 9c) shows a positive trend.

We next examine the linear trends in the key variables for each ice shelf (Fig. 10). At the ice shelves whose linear trend of basal melt rate is higher than +10 cm yr^{-1} century^{-1} (groups A, C–G, and K: LIS, EWIS, SGT, AIS, WeIS/ShIS, ToIS/MGT, and AbIS/GeVI), and at ice shelf H (RIS), the relationships among the variables are similar to

TABLE 1. Definition of Antarctic coastal water masses in this study.

Mode (Jacobs et al. 1992)	Water mass	Potential temperature (°C)	Salinity (psu)
Mode 1	HSSW	$-2.0 \le T < -1.7$	$S \ge 34.6$
	LSSW	$-2.0 \le T < -1.7$	$S < 34.6$
Mode 2	MSW	$-1.7 \le T < -1.0$	$S \ge 34.4$
	MCDW	$T \ge -1.0$	$S \ge 34.4$
Mode 3	ASSW	$T \ge -1.7$	$S < 34.4$
—	ISW	$T < -2.0$	—

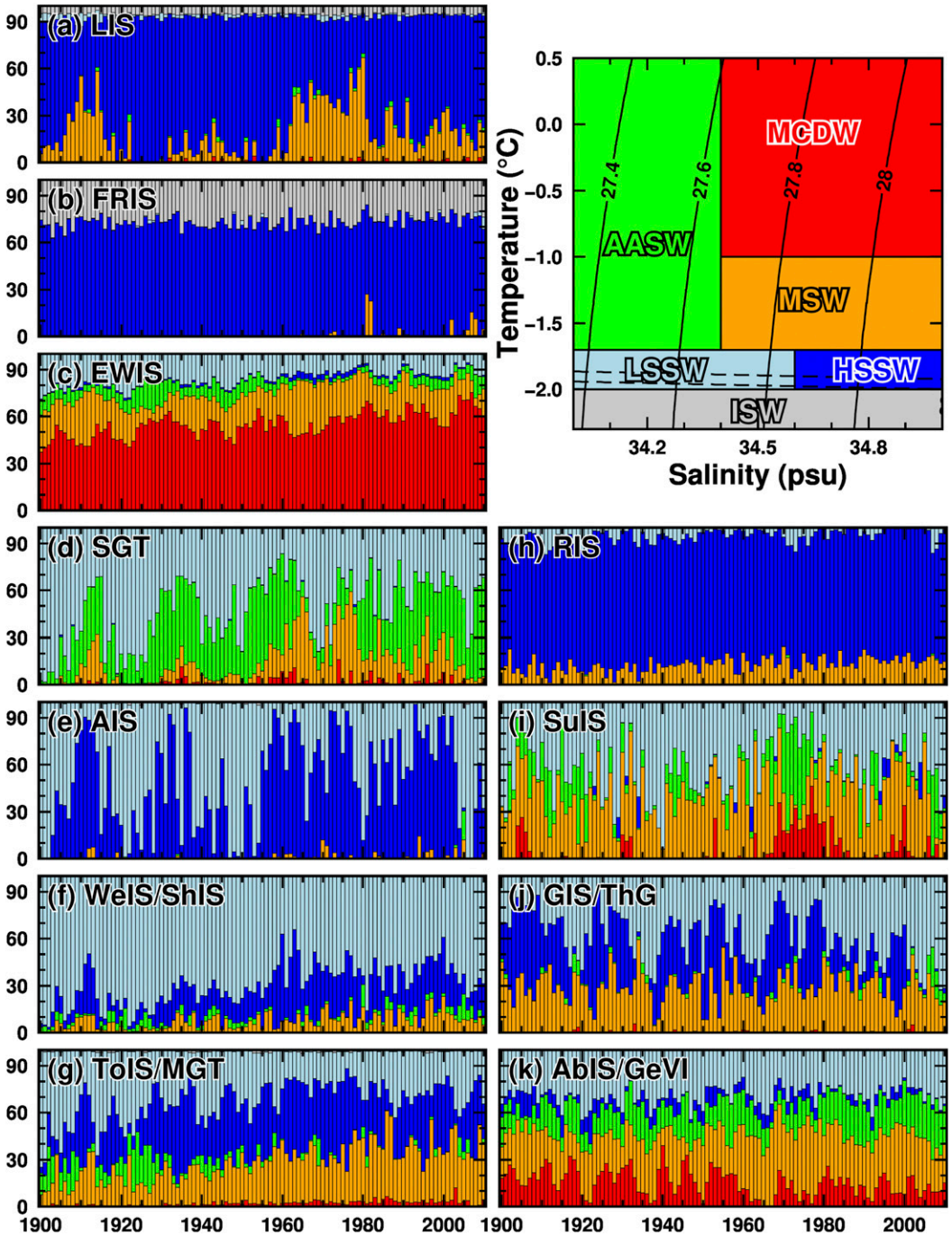

FIG. 8. (a)–(k) Time series of the percentage of Antarctic coastal water masses flowing into each ice shelf cavity in the CTRL case. See Fig. 1 for the locations of the grouped ice shelves (groups A–K). The definition of the water masses shown in Table 1 is illustrated in the top-right *T*–*S* diagram. The contour and dashed lines indicate potential density and freezing temperatures of seawater at the surface and 100-m depth.

those for all of the ice shelves (Fig. 9): a combination of increased transport of warm waters and a reduction of cold water inflow results in mean temperature rises and enhanced ice shelf basal melting during the twentieth century and the early twenty-first century. The increased total heat transport of the water masses is consistent with enhanced large-scale gyre circulation and the associated subsurface warming around

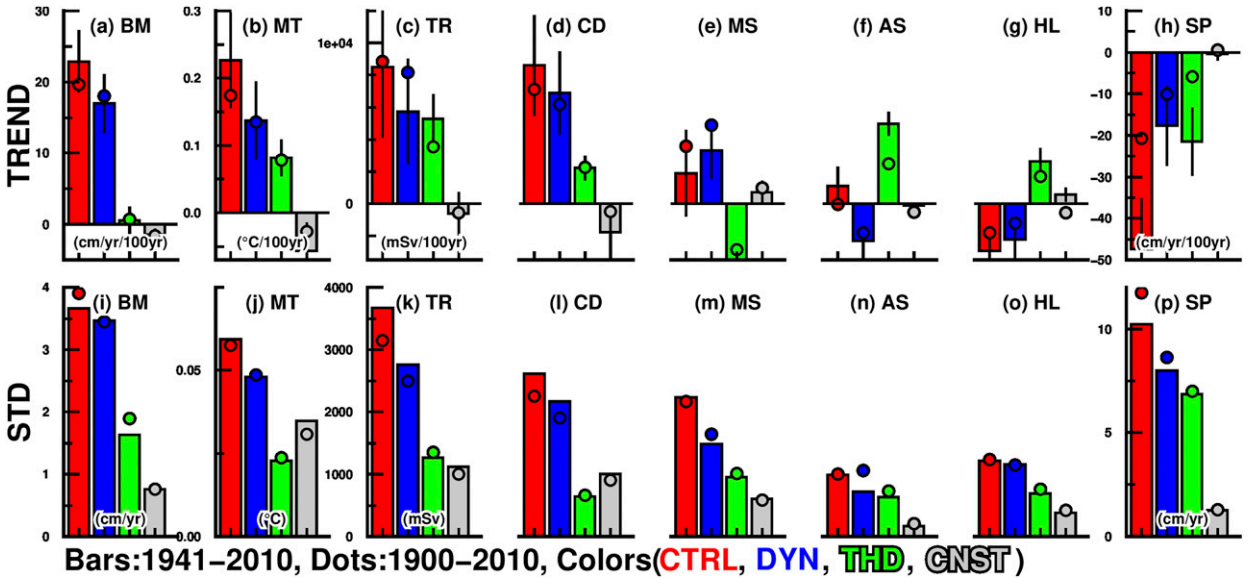

FIG. 9. (a)–(h) Linear trends and (i)–(p) standard deviation of the annual basal melt rate (BM), mean inflow temperature of the total water masses across the ice front (MT), total transport of all water masses (TR), transport of each water mass (CD: Circumpolar Deep Water, MS: Modified Shelf Water, AS: Antarctic Surface Water, and HL: sum of High and Low Salinity Shelf Water), and sea ice production in the neighboring coastal region (SP). Red, blue, green, and gray show results from the CTRL, DYN, THD, and CNST cases, respectively. Bars and dots show the statistics for the periods 1941–2010 and 1900–2010, respectively. The vertical black lines in the top panels indicate 95% confidence level for the trend for the period 1941–2010. The standard deviations are calculated after removing the linear trends.

the shelf break/slope regions (Figs. A8a and A9a), indicating that the stronger gyre circulations bring larger amount of warm water poleward to the Antarctic coastal regions. Substantial increases of AASW are found in ice shelves D (SGT), J (GIS/ThG), and K (AbIS/GeVI) (Figs. 8 and 10) and the positive trend of the AASW transport is consistent with the long-term decline in the actual sea ice days (Fig. A4h).

The ice shelf B (FRIS) shows a different response. Local enhancement of sea ice production (Fig. A5b) results in increased transport of HSSW and LSSW (Fig. 10), indicating the enhanced contribution of the first-mode melting (Jacobs et al. 1992). Since the ice shelf B (FRIS) has deep draft over the extensive area near the grounding line (Timmermann et al. 2010; Schaffer et al. 2016), the increased transport of the cold water masses leads to more active basal melting.

Ice shelves I (SuIS) and J (GIS/ThG) show an insignificant trend of basal melt due to large temporal variability in the mean temperature mainly associated with MSW intrusion (Fig. 8). Therefore, the correlation analysis shown below is more helpful to see the modeled relationship between the variables. It should be noted that (as mentioned before) this model has difficulty in reproducing the observed present-day high basal melt rate in the ice shelf J (GIS/ThG) due to the underestimation of warm water intrusion (Fig. 8).

Along with the long-term linear trends, there is large interannual-to-decadal variability in the coastal water masses flowing to the ice shelf cavities (Fig. 8 and lower panels in Fig. 9). The relationships found in the multidecadal linear trends (Figs. 9 and 10) are also identified in the interannual-to-decadal variability. To confirm the relationship, we calculated correlation coefficients between a pair of the eight variables (ice shelf basal melting, the mean inflow temperature, volume transports of the coastal water masses, and the neighboring sea ice production) for the period 1900–2010. Correlation coefficients for all of the Antarctic ice shelves and each individual ice shelf are shown in Figs. 11 and 12, respectively. The correlation coefficients after the 11-yr running mean are also shown in Fig. 11 to consider the decadal variability. In Figs. 11 and 12, the lines in the vertical axis are variables to be explained and the columns in the horizontal axis are explanatory variables.

As seen in Figs. 11a and 11d, the basal melting has a positive correlation coefficient with the mean temperature ($\geq$0.7), indicating that the mean temperature of water masses flowing into ice shelf cavities is a good indicator of the basal melt variability. The total transport has a significant positive link with the transports of MCDW and MSW (Figs. 11 and 12). Basal melting correlates negatively with the transport of HSSW and LSSW, which is tightly linked with coastal sea ice

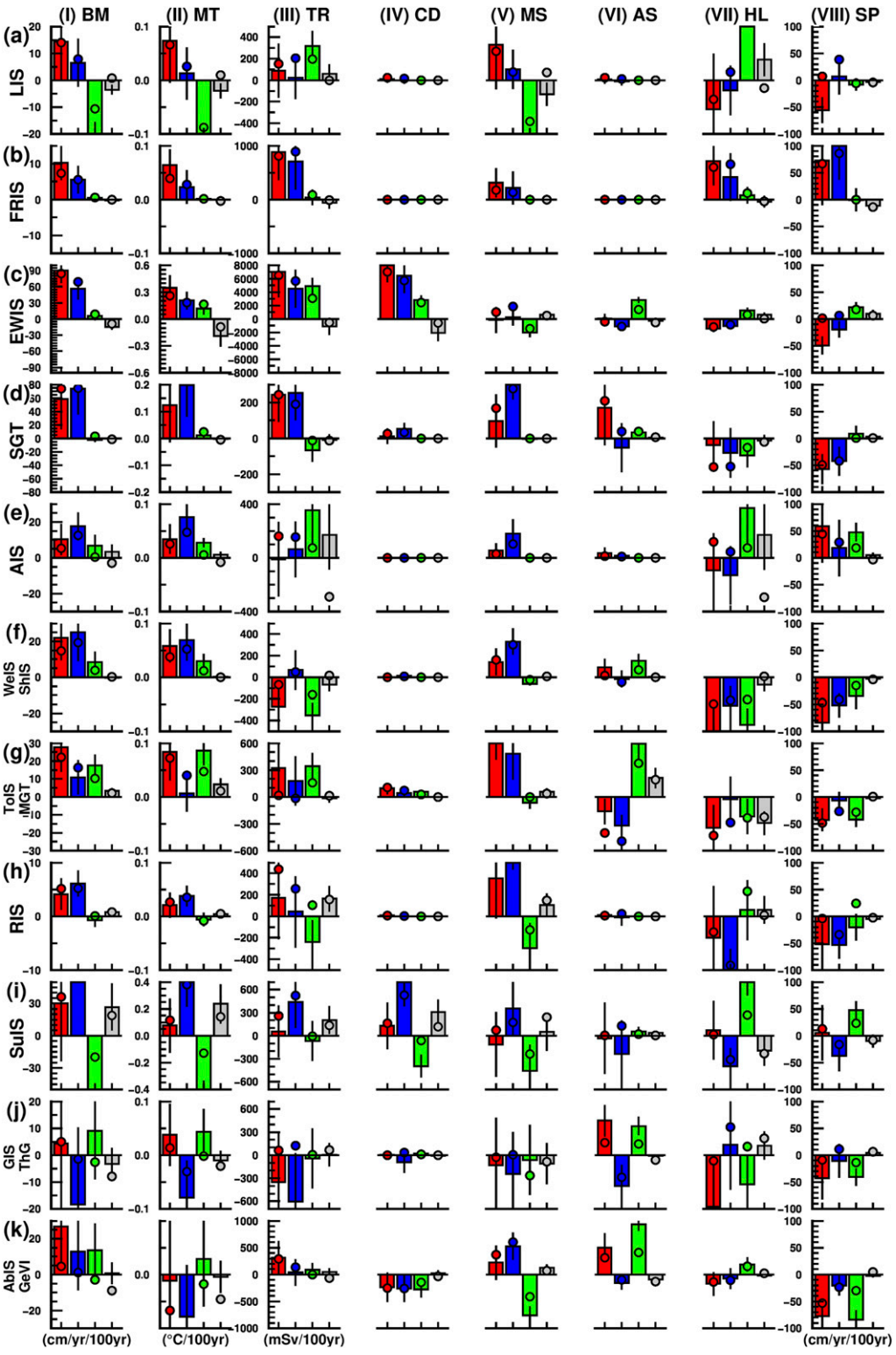

FIG. 10. As in Fig. 9, but for the linear trend, but for each ice shelf group A–K.

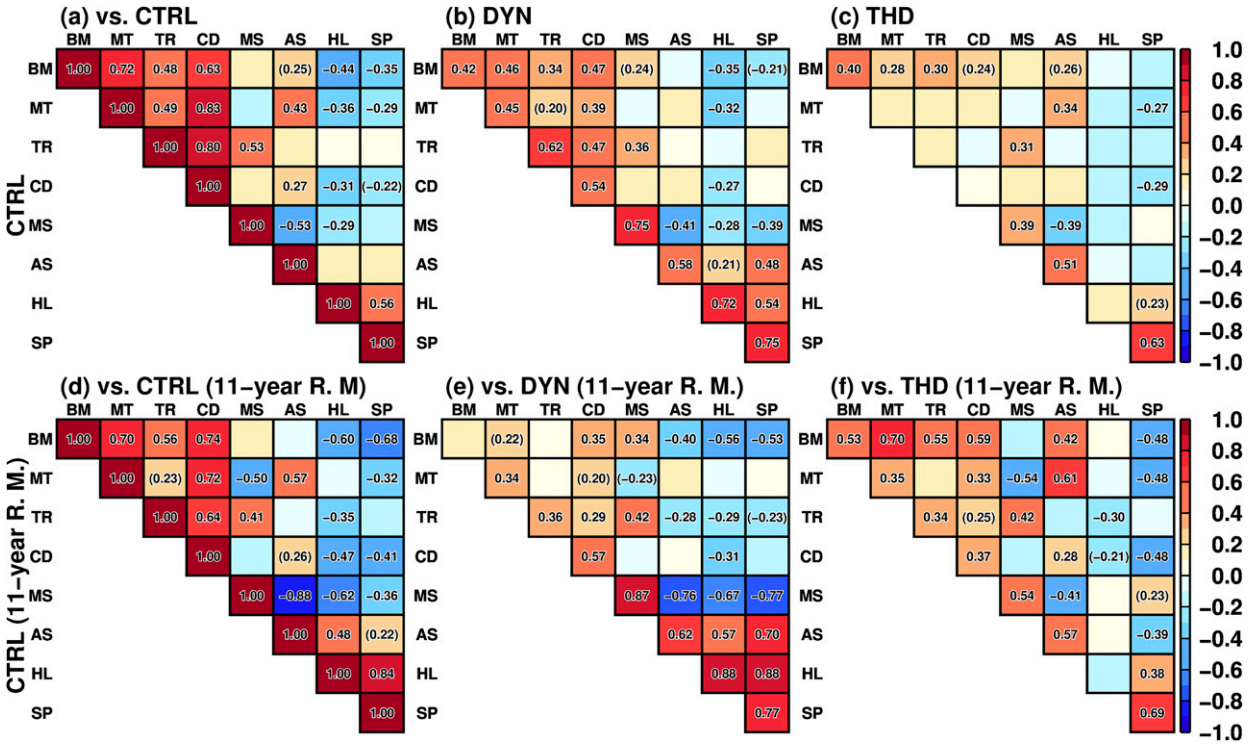

FIG. 11. Correlation coefficients between all combinations of BM, MT, TR, CD, MS, AS, HL, and SP for the period 1900–2010. The lines (in the vertical axis) represent explained variables in the CTRL case and the columns (in the horizontal axis) are explanatory variables in the CTRL, DYN, and THD cases. The correlation was calculated after removing linear trends from the two time series. Results are from (a)–(c) the raw annual data and (d)–(f) 11-yr running mean data. Numbers with and without parentheses show the correlation coefficients that are statistically significant at the 95% and 99% confidence levels, respectively.

production variability (Fig. A5). These relationships become clearer in the decadal variability (Fig. 11d) and can be seen in each ice shelf (left panels in Fig. 12). In ice shelf B (FRIS), the transport of HSSW and LSSW correlates positively with the total transport and the mean temperature. This result again indicates that the cold water masses are a dominant heat source for basal melting there. On the other hand, in other ice shelves, the appearance of cold water reduces the active basal melting caused by warm waters. Looking at ice shelves I (SuIS) and J (GIS/ThG) where the multidecadal trends are insignificant due to the large temporal variability, the basal melting has positive correlations with the mean temperature and transport of the warm waters (MSW or AASW) and negative correlation with sea ice production and volume transport of the cold water.

b. *Responses of ice shelf basal melting and coastal water masses to dynamic and thermodynamic surface forcing*

In this subsection, we examine the factors responsible for the multidecadal linear trends and interannual-to-decadal variability in the ice shelf basal melting and the associated coastal water masses flowing into the cavities. A comparison of the results from three numerical experiments (the CTRL, DYN, and THD cases) allows us to estimate the relative roles of dynamic and thermodynamic surface forcing on the system. Note that in the appendix the same analyses are performed to briefly examine the relative roles in the sea ice and ocean components.

Long-term linear trends in the basal melt rate for all of the ice shelves and each individual ice shelf group from the DYN and THD cases are also plotted in Figs. 9 and 10, along with the trends in the eight key variables. First of all, in this subsection, we examine these trends and the relationship for all of the Antarctic ice shelves (Fig. 9) and then consider in detail the regional characteristics of the trends (Fig. 10). In this study, we use the similarity of the DYN and THD cases to the CTRL case to identify the relative roles of dynamic and thermodynamic forcing. Finally, we show the interannual-to-decadal variability and the links among the variables (Figs. 11 and 12).

Looking at the blue bars in Fig. 9 (results from the DYN case), we can see the effects of dynamic surface forcing on the variables; the warm water masses (MCDW and MSW) show increasing trends in the

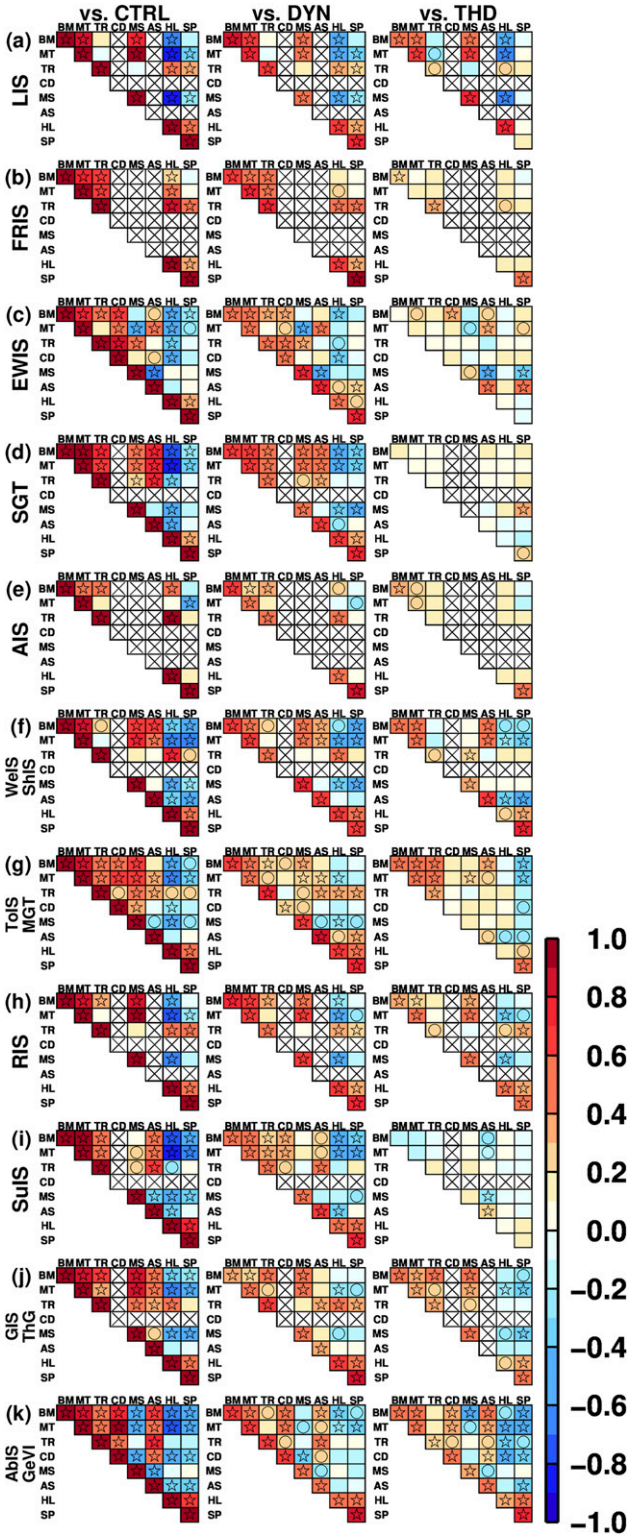

FIG. 12. As in Figs. 10a–c, but for each ice shelf group (A–K). Boxes with circles and stars indicate that the correlation coefficients are statistically significant at the 95% and 99% confidence levels, respectively. Crosses indicate that the length of either or both of the variables is less than a fifth of the total length of the 111 years.

inflow transports while the cold water masses (HSSW and LSSW) show a decreasing trend. These linear trends in the coastal water mass transports contribute to increasing the mean inflow temperature. The enhanced inflow of the warm waters is consistent with the stronger large-scale cyclonic ocean circulation (Figs. A8b,c) and the associated subsurface warming along the Antarctic coastal margins (Figs. A9a,b). The declining trend in the cold waters results from weaker coastal sea ice production (Figs. A5b,c), which is linked with the weakened easterly coastal wind (Figs. 2d,e). The magnitude of the positive trends for the warm water inflow is larger than that of the negative trend for the cold water, and thus the total transport shows a positive trend. Overall, results from the CTRL case are similar to those from the DYN case, indicating that dynamic surface forcing is the main responsible factor for the long-term linear trends in the basal melting of Antarctic ice shelves over the twentieth century and the early twenty-first century.

Looking at the green bars in Fig. 9 (results from the THD case), there are positive trends in the MCDW and AASW inflow volume transports, while the MSW transport has a negative trend. The tendencies in the MCDW and AASW transport would lead to a higher basal melt rate, although the opposite trends in the MSW transport partially reduce the effect. The volume transport of the cold water masses (HSSW and LSSW) shows positive trends, while the total sea ice production has negative trends. This counterintuitive result comes from the large regional variability in the sea ice production (Fig. A5d) and subsurface temperature (Fig. A9c), explained in more detail below. The increased transport of the cold water masses in the THD case contributes to the positive trend in the total volume transport in the experiment. The trend in the mean temperature of the inflow in the THD case is positive because the contributions of warm waters from MCDW and AASW compensate for the MSW reduction and the cold-water increase. The basal melt rate trend in the THD case is a very small (statistically insignificant) positive trend, while that in the DYN case is large enough to explain the results in the CTRL case. This result indicates that trends in both the mean temperature and warm-water inflow transports; in other words, the heat flux into the cavities is essential for understanding the basal melt at all of the Antarctic ice shelves.

Figure 10 illustrates regional trends in the basal melt rate and the key variables in the three experiments. Judging from the trend patterns in the basal melt rate, the mean temperature, and the total inflow volume transport, we can classify the ice shelf groups into two regimes: a group of wind stress controlling ice–ocean interaction (the W-regime) and a group in which ice–ocean interaction is controlled by the combination of dynamic and thermodynamic surface forcing (the C-regime). The ice shelf groups A–E and H (LIS, FRIS, EWIS, SGT, AIS, and RIS) are categorized into the W-regime. In most of the ice shelf groups in the W-regime, there is a positive trend in the MSW/MCDW volume transport and a negative trend in the HSSW and LSSW volume transport. In ice shelf group B (FRIS), wind stress enhances the inflow volume transport of cold water, leading to an increase in the total volume transport. In these ice shelves, the result from the THD case does not account for the trends in the CTRL case (small or opposite tendencies). These results indicate that wind stress is a dominant driver for the regional trends. It should be noted that while the trend of coastal sea ice production near the ice shelf A (LIS) is almost zero (small negative) in the THD case, the trend in the volume transport of the cold water masses is positive. The counterintuitive results in the THD case are partially explained by the enhanced sea ice production and cold water masses in the offshore region in the Weddell Sea (Figs. A5d and A9c), which is outside of the defined coastal areas in the analysis.

The ice shelf groups F, G, and I–K (WeIS/ShIS, ToIS/MGT, SuIS, GIS/ThG, and AbIS/GeVI) are categorized into the C-regime where the linear trends in the basal melt rate, the mean temperature, and the total volume transport from the THD case are comparable to or higher than those from the CTRL and DYN cases, indicating that thermodynamic surface forcing is also responsible for the trends. Looking at the AASW transport trends in the THD case, significant positive trends are found in the ice shelves C, F, G, J, and K (EWIS, WeIS/ShIS, ToIS/MGT, GIS/ThG, and AbIS/GeVI). These ice shelves roughly correspond to regions of later sea ice advance or early sea ice retreat (Figs. A4b,e). The results indicate that these ice shelves are potentially sensitive to the AASW changes, which link with the sea ice processes.

The rest of this subsection examines the relationships of interannual-to-decadal variability in basal melt rate and the key variables (Fig. 11). To do this, we calculated cross-correlation coefficients between a pair of the eight variables in the CTRL and DYN/THD cases. Correlation coefficients on the diagonal line for the same variables between the CTRL and DYN cases (Fig. 11b) show significant positive correlations for all of the variables, while those between the CTRL and THD cases are significantly positive only in the basal melt rate and transports of MSW and AASW, and sea ice production (Fig. 11c). The correlation coefficients

with the THD case are smaller than those in the DYN case. Looking at the relationship in the decadal variability (Figs. 11e,f), the correlation coefficients with the THD case become more significant in the variables (mean temperature, volume transport of water masses, and sea ice production). This result indicates that along with dynamic forcing, thermodynamic surface forcing contributes to the low-frequency variability of the coastal water masses and ice shelf basal melting.

The same correlation analysis was applied to each ice shelf group (Fig. 12). The pattern similarity of the correlation coefficients in the CTRL case to those in the DYN and THD cases enables us to identify the responsible factors for the temporal variability. Overall, the magnitude of the correlation coefficients with the DYN case is higher than those with the THD case, indicating dynamic forcing is a dominant factor for determining the interannual-to-decadal variations in Antarctic ice shelf basal melting and coastal conditions.

5. Summary and discussion

We have investigated the ocean and cryosphere over the Southern Ocean throughout the twentieth century and the early twenty-first century (1900–2010), based on results from an ocean–sea ice–ice shelf model forced with a long-term atmospheric reanalysis dataset (Fig. 2; ERA20C; Poli et al. 2016). Consistent with the observational sea ice evidence, the model shows that Antarctic sea ice extended farther northward in the early twentieth century, then started to shrink in the 1940s, and settled at the present-day level after about 1980 (Figs. A1–A3). The annual timings of sea ice advance and retreat, actual ice days, and sea ice production also changed greatly in this period (Figs. A4 and A5). The ocean component captured the spatial and temporal variability of the Southern Ocean SST (Fig. A6). Furthermore, the modeled trend of zonal mean temperature for the period 1900–2010 (Fig. A7) is similar to the decadal trend derived from the observation dataset (Armour et al. 2016; Swart et al. 2018). The validation of the modeled sea ice and ocean fields gives us some confidence in using the model results to examine changes in Antarctic coastal water masses and ice shelf basal melting.

Although the century-scale atmospheric reanalysis dataset is useful for driving ocean–sea ice–ice shelf models, we must keep in mind that the atmospheric conditions over the Southern Ocean in the ERA20C system are less constrained than those in the tropics and Northern Hemisphere due to a lack of observations (Poli et al. 2016). The uncertainties in the forcing entail uncertainties in the model results. We have assessed the representation of spatiotemporal variability in surface air temperature (Figs. 2, 3, and 5) and temporal variability in the SAM index (Figs. 3 and 4) for the period 1900–2010 by comparing with the available observations. It is found that the atmospheric conditions in ERA20C after the 1940s are consistent with the observational evidence to some extent, although the positive SAM trend and warming trend appear to be overestimated (Fig. 3).

We have performed the first detailed analysis of multidecadal trends and interannual-to-decadal variability in basal melting at the Antarctic ice shelves and have shown linkages between ice shelf melting and sea ice/ocean processes. Including the uncertainties in the atmospheric forcing, our model shows that Antarctic ice shelf basal melting increased about 1.5-fold from 700 to 1100 $\mathrm{Gt\,yr^{-1}}$ over the study period 1900–2010 (Fig. 6). Changes in ocean heat flux into the Antarctic ice shelf cavities can explain the long-term trends and the interannual-to-decadal variability in the basal melting (Figs. 8–12). A series of numerical experiments allow us to identify the responsible factors for changes in Antarctic coastal water masses flowing into the ice shelf cavities and ice shelf basal melting. It is found that dynamic surface forcing is the main factor for determining Antarctic ice shelf basal melting. Changes in wind stress over the Southern Ocean (Fig. 2) cause enhanced poleward heat transport to the Antarctic coastal margins by stronger subpolar gyres (Figs. A8 and A9) and further modify regional sea ice and cold-water formation. These changes lead to modification of the coastal water masses flowing into the ice shelf cavities and increase the contribution of warm waters, resulting in the enhanced basal melting (Figs. 8–10). On the other hand, consistent with the century-scale warming trend over the Southern Ocean (Fig. 2h), thermodynamic surface forcing partially contributes to increased basal melt through changes in AASW and coastal cold-water formation (Figs. 8–10).

There are several studies that have focused on future projections of Antarctic ice shelf basal melting. For example, Hellmer et al. (2012) and Timmermann and Hellmer (2013) utilized ocean–sea ice–ice shelf models forced with surface boundary conditions derived from future warming scenarios and demonstrated that a redirected coastal current in the southeastern Weddell Sea could be a trigger for an abrupt increase of basal melting in the Filchner–Ronne Ice Shelf cavity. Naughten et al. (2018) also performed similar numerical experiments and showed that an increased presence of warm CDW on the Antarctic continental shelf enhances basal melting under a warming climate of the twenty-first century. Kusahara and Hasumi (2013) conducted a series of idealized warming experiments and concluded that water masses flowing into ice shelf cavities differ greatly

between Antarctic ice shelves and the changes in the inflowing water masses are responsible for the basal melt changes in the experiments. This study and all of the above studies clearly show that changes in coastal water masses over the Antarctic continental shelf are essential for understanding basal melt of Antarctic ice shelves, supporting the idea that the changes in Antarctic coastal water masses are one of the most important metrics for understanding Antarctic and Southern Ocean climates (Bracegirdle et al. 2016).

Acknowledgments. This work was supported by the Integrated Research Program for Advancing Climate Models (TOUGOU program) from the Ministry of Education, Culture, Sports, Science and Technology (MEXT), Japan, and JSPS KEKENHI Grants JPMXD0717935715, JP19K12301, JP17H06323. All the numerical experiments with the ocean–sea ice–ice shelf model were performed on HPE Apollo6000XL230k Gen10 (DA system) in JAMSTEC and the Fujitsu PRIMERGY CX600M1/CX1640M1 (Oakforest-PACS) in the Information Technology Center, The University of Tokyo. I am grateful to Dr. Paul Spence and three anonymous reviewers for their careful reading and constructive comments on the manuscript.

APPENDIX

Representation of Sea Ice and Ocean Fields and the Responses to Dynamic and Thermodynamic Forcing

a. *Representation of sea ice and ocean fields in the CTRL case*

1) SEA ICE

Since sea ice is an interface between the high-latitude atmosphere and ocean, it plays important roles in the climate at regional-to-global scales. The Southern Ocean is the greatest seasonal sea ice cover zone, whose extent varies from $3.1 \times 10^6\,km^2$ in summer to $18.5 \times 10^6\,km^2$ in winter in the present day (Parkinson and Cavalieri 2012), and whose sea ice–related processes (e.g., salt rejection in coastal regions and freshwater transport to remote regions by sea ice) control seasonal and interannual/decadal changes in the seawater properties over the Southern Ocean.

This study uses results from an ocean–sea ice–ice shelf model forced with reanalysis-based atmospheric surface boundary conditions. Here, we would like to discuss the utility of the ocean–sea ice model forced by the surface boundary conditions. Although the ERA20C reanalysis system did not assimilate the observed sea ice and sea surface temperature in the product, it used them for specifying the atmospheric bottom boundary conditions. This fact indicates that the observed sea ice edge is imprinted in the atmospheric surface boundary conditions for the ocean–sea ice model, and one can speculate that an ocean–sea ice model forced with such surface boundary conditions does reproduce sea ice extent to some extent. An ocean–sea ice model intercomparison study by Downes et al. (2015) reported that multiple ocean–sea ice models forced with exactly same atmospheric surface boundary conditions can reproduce the observed seasonal cycle of Antarctic sea ice, but there are large differences in long-term trends of the sea ice edge and interior sea ice concentration among the models. Therefore, even if the ocean–sea ice model is forced with the reanalysis-based surface conditions, it is essential for this study to assess the sea ice representation in the model to have some confidence in the analyses for Antarctic coastal water masses and basal melt at ice shelves in the main text.

For convenience, we divided the integration period into three periods (1901–40, 1941–80, and 1981–2010) to show the seasonal cycle and distribution of Antarctic sea ice (Figs. A1 and A2). Reliable sea ice concentration (SIC) measurements from satellite passive microwave data have been available since the late 1970s, and we can compare the modeled SIC with the observations for the most recent period (1981–2010). We used the daily observed SIC derived from satellite passive microwave data by the NASA Team algorithm (Cavalieri et al. 1984; Swift and Cavalieri 1985). This study used a threshold value of 15% SIC for defining the sea ice extent (SIE) and edge.

The sea ice model has a reasonable performance in reproducing the observed seasonal cycle of the total sea ice extent (black and red lines in Fig. A1) and the SIC distribution for the third period 1981–2010 (Figs. A2a–d,e–h). Note that there are some model biases: an underestimation of the total SIE in summer and an overestimation in winter. Similar sea ice model biases were reported in detail in our previous studies (Kusahara et al. 2019), which used the same model but with a different model configuration and surface boundary conditions (ERA-Interim for 1979–2014). Although there exist some biases, the CTRL case reproduces the spatiotemporal seasonal pattern of the observed SIC for the period 1981–2010, providing confidence in the ability of the model to represent sea ice behavior in the early- and the mid-twentieth century (Fig. A2) and the related ocean processes. Throughout the model integration, the seasonal cycle of the SIE (minimum in February and maximum in September) is the same, but the amplitudes of the seasonal cycle in the first and second periods ($4.7–25.9 \times 10^6\,km^2$ for 1901–40 and $3.1–23.1 \times 10^6\,km^2$ for 1941–80,

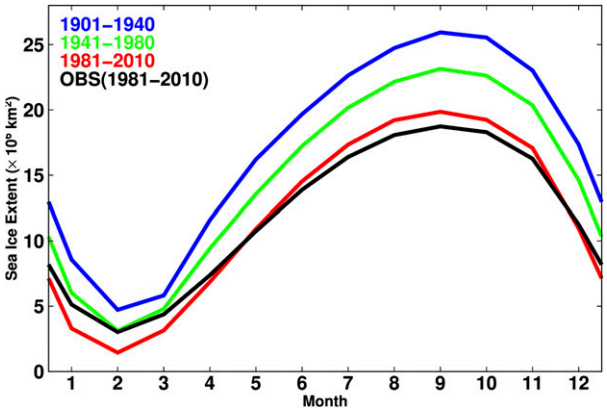

FIG. A1. Seasonal variation of total Antarctic sea ice extent (SIE). Black and colored lines indicate the observed monthly SIE averaged over 1981–2010 and the modeled SIE from the CTRL case for three different periods (blue: 1901–40, green: 1941–80, red: 1981–2010), respectively.

respectively) are more extensive than that in the third period (1.5–19.9 $\times$ 10^6 km^2 for 1981–2010).

Looking at the SIC distributions in the early-twentieth century (Fig. A2m–p), sea ice exists at almost all longitudes even in summer, and in particular, the sea ice edge in the Weddell Sea extends farther northward than that in recent decades (Figs. A2e–h). The difference in the sea ice edge between the two periods becomes more prominent from autumn to spring (~7° of latitude in spring). In the mid-twentieth century (1941–1980; Figs. A2i–l), the spatial pattern of the SIC anomaly from the SIC in the period 1981–2010 is similar to that in the early-twentieth century, but the amplitude of the anomaly is smaller (e.g., ~5° of latitude in spring).

The winter maximum, annual mean, and summer minimum SIEs are shown in Fig. A3a to indicate the time evolution of the total SIE throughout the model integration (1900–2010). Century-scale time series of the total SIE estimated from the HadISST dataset (Rayner et al. 2003) are also shown to assess the sea ice model performance (gray lines in Fig. A3a). Note again that the ERA-20C assimilation system used sea surface temperature (SST) and SIC derived from the HadISST dataset to specify lower boundary conditions for the system (but they are not assimilated variables). All three metrics show long-term decreasing trends in the twentieth century. The model has a systematic underestimation in the summer total SIE. SIEs in the first and the third periods are relatively stable and have high and low SIEs, respectively. The mid-twentieth century is the transition from high to low SIE. Note that the magnitude of the SIE reduction in the winter (approximately 6 $\times$ 10^6 km^2) is larger than that in summer (3 $\times$ 10^6 km^2). It is known from several fragmentary pieces of evidence, such as historical whaling records (de la Mare 1997; Cotté and Guinet 2007), proxy reconstructions (Curran et al. 2003; Abram et al. 2010; Murphy et al. 2014), and rescued satellite images in the 1960s and the early 1970s (Cavalieri et al. 2003; Meier et al. 2013), that the Antarctic sea ice edge in the early and middle twentieth century was located farther northward than that in recent decades. Numerical modeling results also support the long-term decline in Antarctic sea ice in the twentieth century (Goosse et al. 2009; Gagné et al. 2015; Hobbs et al. 2016b). Our sea ice model results are consistent with the findings from these previous observational and modeling studies.

Here we use three metrics (annual timing of sea ice advance, retreat, and actual ice days) to further examine the seasonal rhythms of the Antarctic sea ice. These sea ice metrics have been used often in satellite-based observational studies (Stammerjohn et al. 2008, 2012; Massom et al. 2013) and are also useful for examining the seasonal behavior of the modeled sea ice (Kusahara et al. 2019). Following the definition of the previous studies (e.g., Stammerjohn et al. 2008), we calculated the timings of sea ice advance and retreat, and actual ice days for the period 1900/01–2009/10, and estimated the mean, linear trend, and standard deviation (Fig. A4). Only the regions where the temporal data coverage is greater than 80% are shown in the figure, and thus the plotted regions roughly correspond to the winter sea ice maximum in recent decades (Fig. A2g). Looking at the maps of the linear trends (Figs. A4b,e,h), the linear trends are statistically significant at the 99% level over most of the Southern Ocean, with a few exceptions (central pack ice regions in the Ross Sea, coastal regions in the Amundsen and Bellingshausen Seas, and near ice edge regions in the Amundsen Sea). In the sea ice edge and central regions from the Weddell Sea to the southeastern Indian Ocean, the sea ice advance begins about 90 days later. The region from 80° to 210°E and the Bellingshausen Sea show a 40–50-day later advance. Regarding the timing of sea ice retreat, the Weddell Sea shows the largest reduction in the retreat onset of around 60–90 days, while the other sectors (except the region from the eastern Ross Sea to the Amundsen Sea) show a 30–60-day earlier retreat. The combination of the later advance and earlier retreat results in 60–150 fewer actual ice days in the edge regions of the winter sea ice maximum (except the Amundsen Sea, where both the trends in the timings of the advance and retreat are not significant). Looking at the maps of the variability fields (Figs. A4c,f,i), a large variability in the advance is found in the region from the western Pacific Ocean eastward to the Antarctic Peninsula with a maximum signal of 30–50 days in the Amundsen-Bellingshausen Sea region; similar patterns are also found in the variability of the retreat and actual ice days.

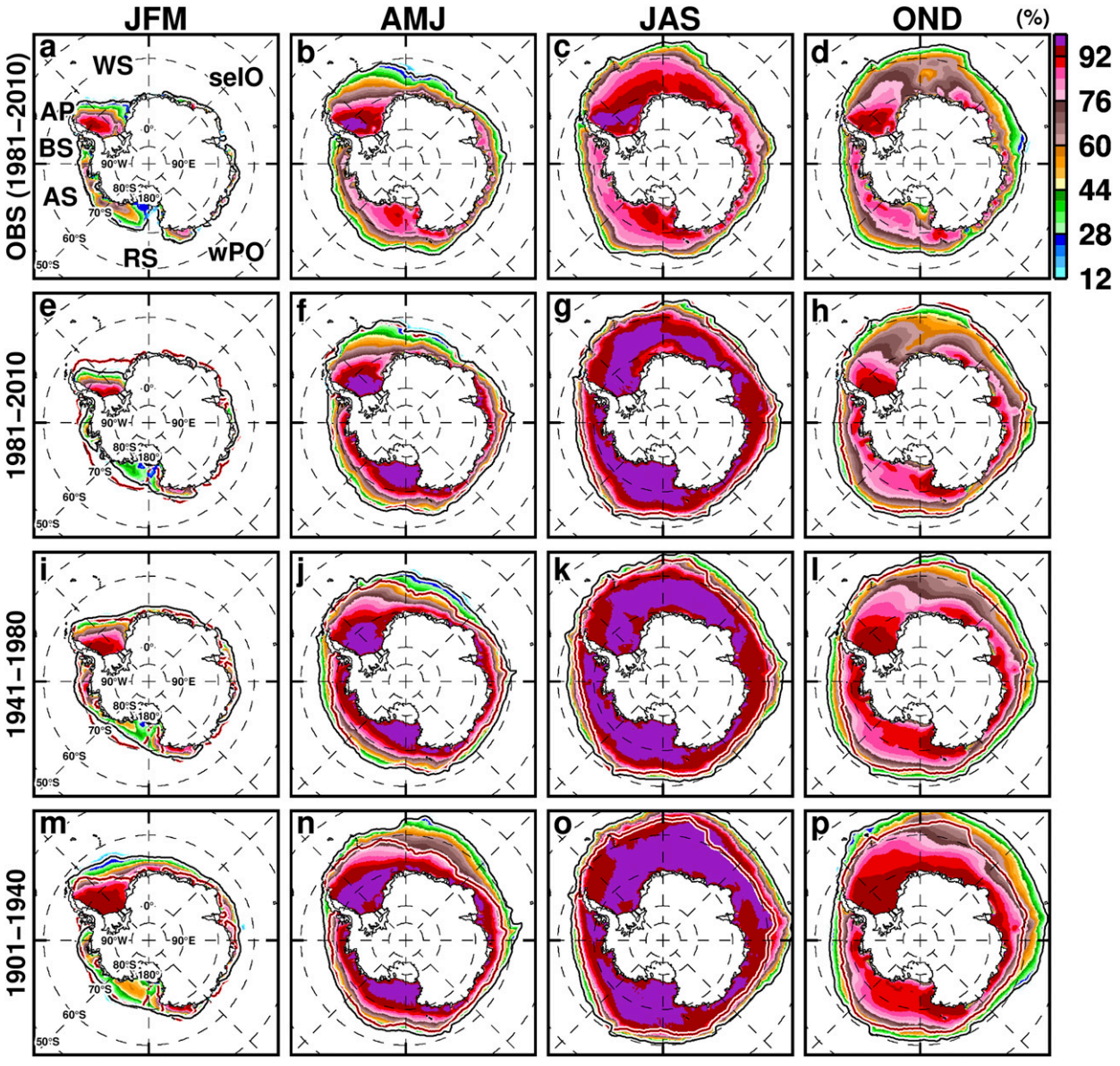

FIG. A2. Maps of seasonal sea ice concentration (SIC) in (a)–(d) observations and (e)–(p) models. The observed SIC (estimated with the NASA team algorithm) was averaged for the period 1981–2010. The modeled SIC was divided into three periods and averaged over the periods 1981–2010 in (e)–(h), 1941–80 in (i)–(l), and 1901–40 in (m)–(p). Black lines indicate the sea ice edge that was defined by the 15% contour. Red lines in the model results in (e)–(p) show the observed sea ice edge for the period 1981–2010.

Next, we show maps of the modeled sea ice production (Fig. A5), because the sea ice production is a key parameter for water mass formation along Antarctic coastal margins (Morales Maqueda et al. 2004). In the coastal regions (where the water depth is shallower than 1000 m), several active sea ice formation regions are reproduced in the model (Fig. A5a) and the spatial pattern is consistent with the satellite-based observations (Tamura et al. 2008; Nihashi and Ohshima 2015) and our previous modeling studies (Kusahara et al. 2017b). Looking at the trend of sea ice production, the Antarctic coastal regions show an overall decreasing trend in sea ice production, but in some regions (e.g., coastal regions in front of the Filchner–Ronne, Amery, and eastern Ross Ice Shelves) an increasing trend is found. There is a circumpolar negative trend in the offshore regions, and this is consistent with the long-term declining trend of sea ice extent (Fig. A3).

2) OCEAN

Ocean heat flux into the ice shelf cavities (which are insulated from the atmosphere) is the only heat source

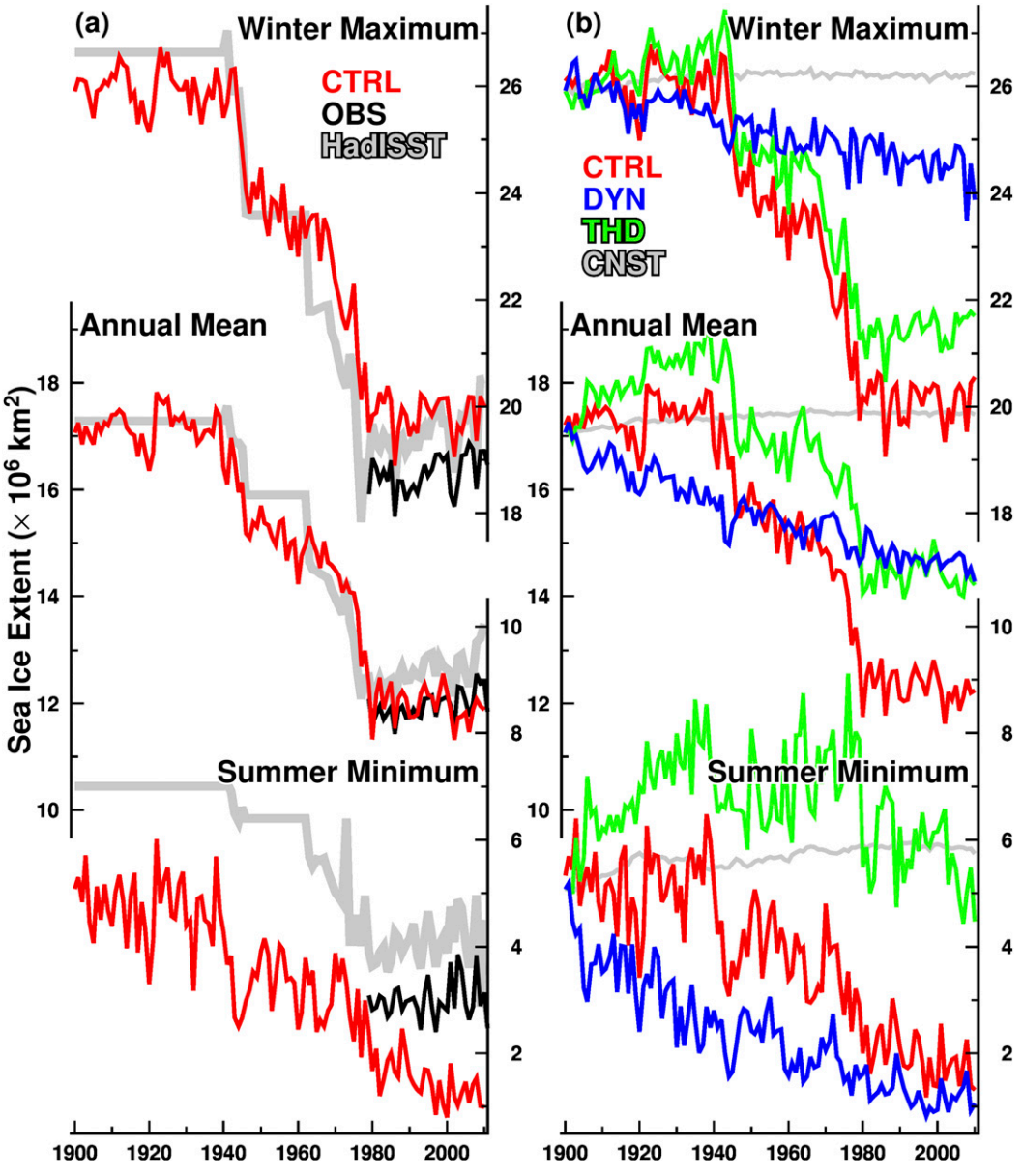

FIG. A3. Time series of the (top) winter maximum, (middle) annual mean, and (bottom) summer minimum in the total sea ice extent. (a) Results from the CTRL case (red) and observation (black: SIE with NASA team algorithm, gray: SIE from HadISST dataset) and (b) results from the numerical experiments (blue: DYN case, green: THD case, and gray: CNST case).

for melting at Antarctic ice shelf bases. Therefore, the model's representations of ocean temperature and circulation are essential for understanding Antarctic water mass formation and their impact on the cryosphere over the Southern Ocean. In this subsection, we show the modeled SST (and a comparison with an observation-based dataset) and vertical sections of zonally averaged potential temperature to examine large-scale Southern Ocean temperature fields (Figs. A6 and A7), and then we utilize maps of the vertically integrated transport (barotropic) streamfunction (Fig. A8) and subsurface temperature (Fig. A9) to assess basin-scale changes in ocean circulation and temperature in the model.

The model shows a long-term warming trend in zonally averaged SST for the period 1900–2010, but with some temporal and regional biases (Fig. A6). The HadISST dataset shows a gradual increase in the zonally averaged SST for the period 1900–80 with an amplitude of about 0.5°C from 1.6° to 2.1°C, and it becomes relatively stable (a slight cooling trend) during the late

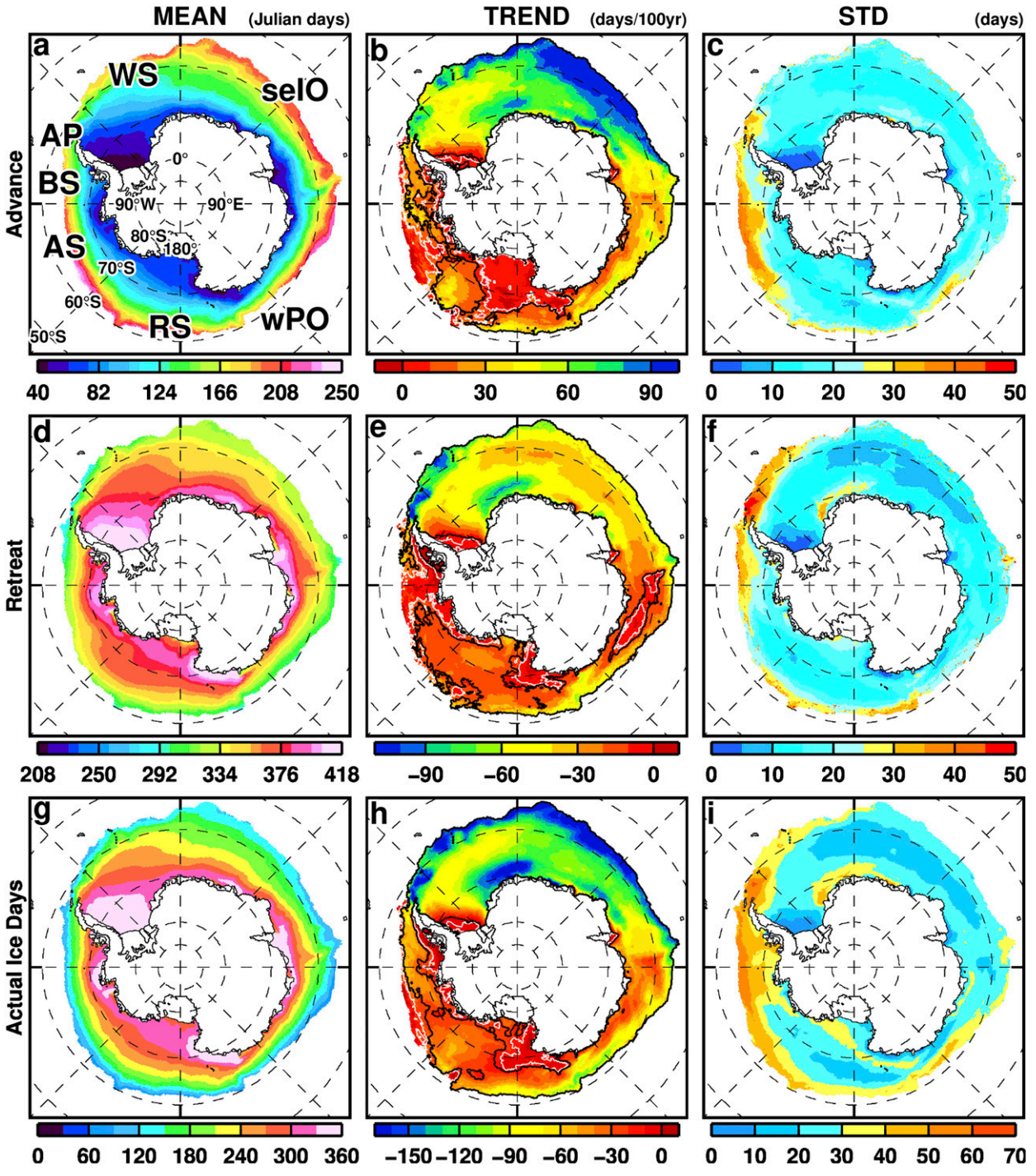

FIG. A4. Maps of the annual timings of sea ice (top) advance and (middle) retreat, and (bottom) actual ice days for the period 1900/01–2009/10 in the CTRL case: (a),(d),(g) the climatology/mean, (b),(e),(h) the linear trend, and (c),(f),(i) the standard deviation after removing the linear trend. In the calculation of the advance and retreat timings, the annual search window is defined from the Julian day 46 (mid-February) to 410 (411 for leap years) in the next year to take account of the seasonal cycle of the Antarctic sea ice. In the panels for the linear trend, black and white contours show the 99% and 90% significant levels, respectively.

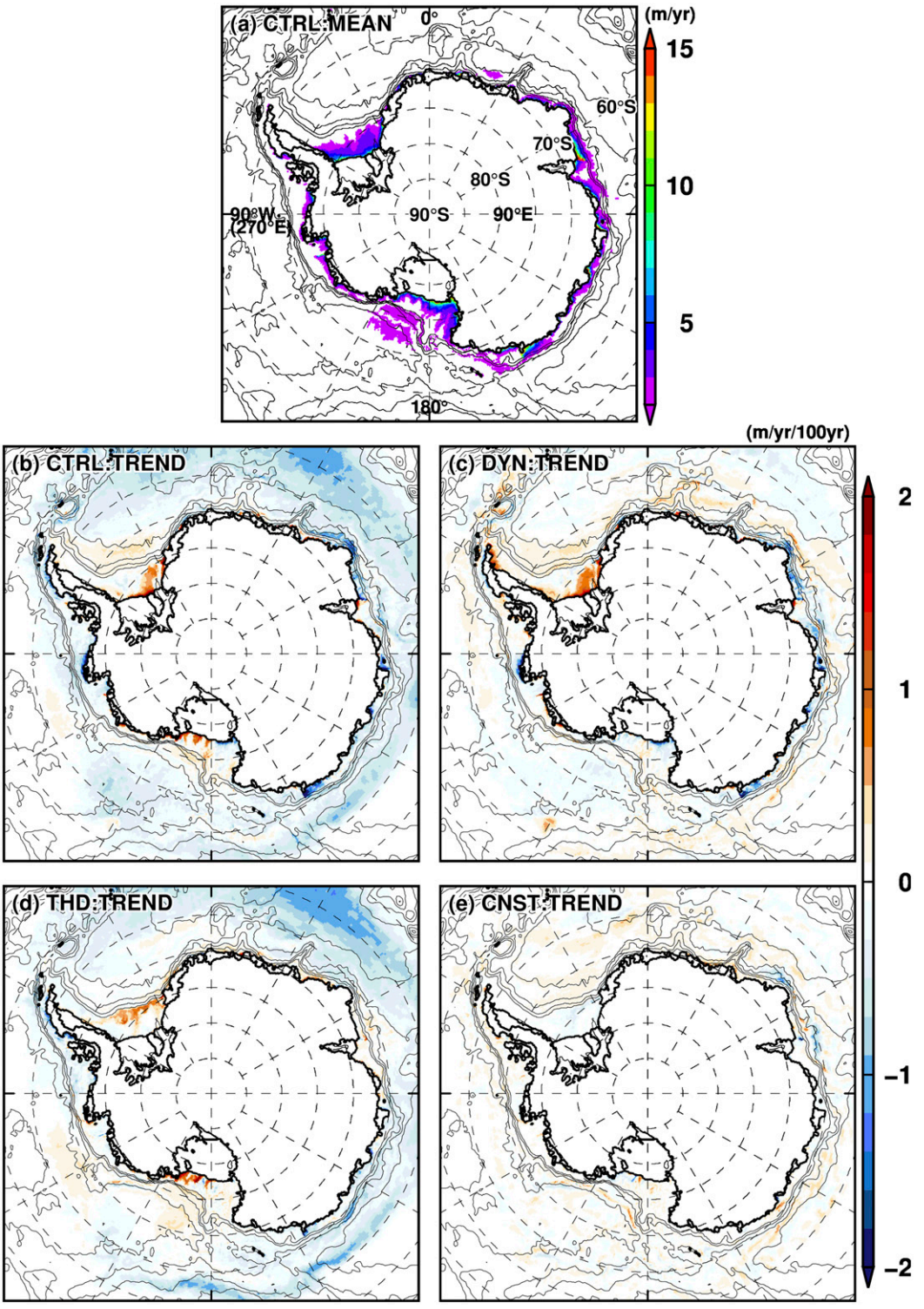

FIG. A5. Maps of (a) annual mean sea ice production in the CTRL case and (b)–(e) the linear trends for the period 1900–2010 in the experiments [CTRL case in (b), DYN case in (c), THD case in (d), and CNST case in (e)]. In (a), areas of sea ice production less than 2 m yr^{-1} are masked out. The black lines show the depth contour at 1000-m intervals.

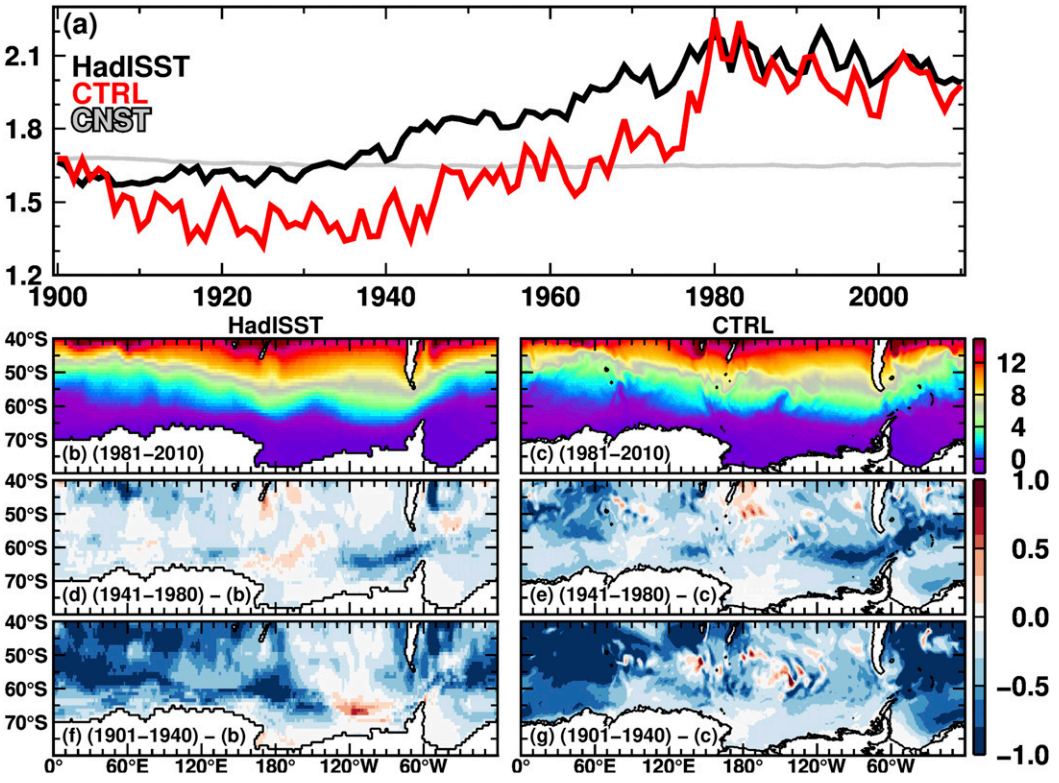

FIG. A6. Time evolution of SST over the Southern Ocean for the period 1900–2010. (a) Zonal mean SST averaged over the latitudes between 50° and 70°S (black: HadISST dataset, red: CTRL case, and gray: CNST case). (b),(c) Maps of annual mean SST averaged over the period 1981–2010 for the HadISST dataset and CTRL case, respectively. Maps of SST for the periods (d),(e) 1941–80 and (f),(g) 1901–40 in the HadISST dataset and CTRL case, respectively, are shown with deviation from the 1981–2010 climatology.

twentieth and early twenty-first century. On the other hand, the CTRL case shows a weak cooling trend during the early twentieth century (1900–20), then relatively stable SST (a slight cooling trend) in the period 1920–40, a pronounced warming trend in the period 1941–80, and again stable SST in the period 1981–2010. A comparison of the results in the CTRL and CNST case shows that the temporal SST change is not model drift or instinct variability, and it is a response to the atmospheric surface boundary conditions. Time series of the observed and reanalyzed air temperature over the Southern Ocean (Fig. 5b) also show a similar time evolution of the modeled SST for the period 1900–2010. The SST difference between the model and HadISST dataset may indicate a small contribution of the atmospheric bottom boundary conditions in the ERA20C system to the reanalyzed atmospheric surface conditions (i.e., atmospheric circulation change predominating the reanalyzed fields).

Looking at regional SST in the period 1901–40 (referenced against the SST climatology for 1981–2010), the model reproduces the large-scale patterns: colder SST in the Atlantic and Indian sectors and extensive areas of small warmer/nearly-zero SST from the Amundsen Sea to the Antarctic Peninsula. The colder SST in the model is broader than in the HadISST dataset (particularly, in the Atlantic sector), contributing to the difference in the time series of the zonally averaged SST (Fig. A6a). The SST in the period 1941–80 shows a similar pattern, but with smaller magnitudes (Figs. A6d,e).

We next show vertical profiles of zonally averaged potential temperature to see how the model represents the Southern Ocean water masses at the surface (0–100 m), subsurface (100–500 m), and intermediate depths (500–2000 m) (Fig. A7). Pronounced warming trends are identified at depths from the surface to 2000 m north of 60°S (Fig. A7b). The maximum of the warming trends exists between 27.2 and 27.4 kg m^{-3} of the potential density surfaces. Just north of the warming trend (north of 40°S), there is a cooling trend in the subsurface layer. These trend patterns of the zonally averaged temperature are broadly similar to the observed trends in recent decades (Armour et al. 2016; Swart et al. 2018). The analysis period of Armour et al. (2016) was 1982–2012. Figure A7f shows the temperature trend for the recent

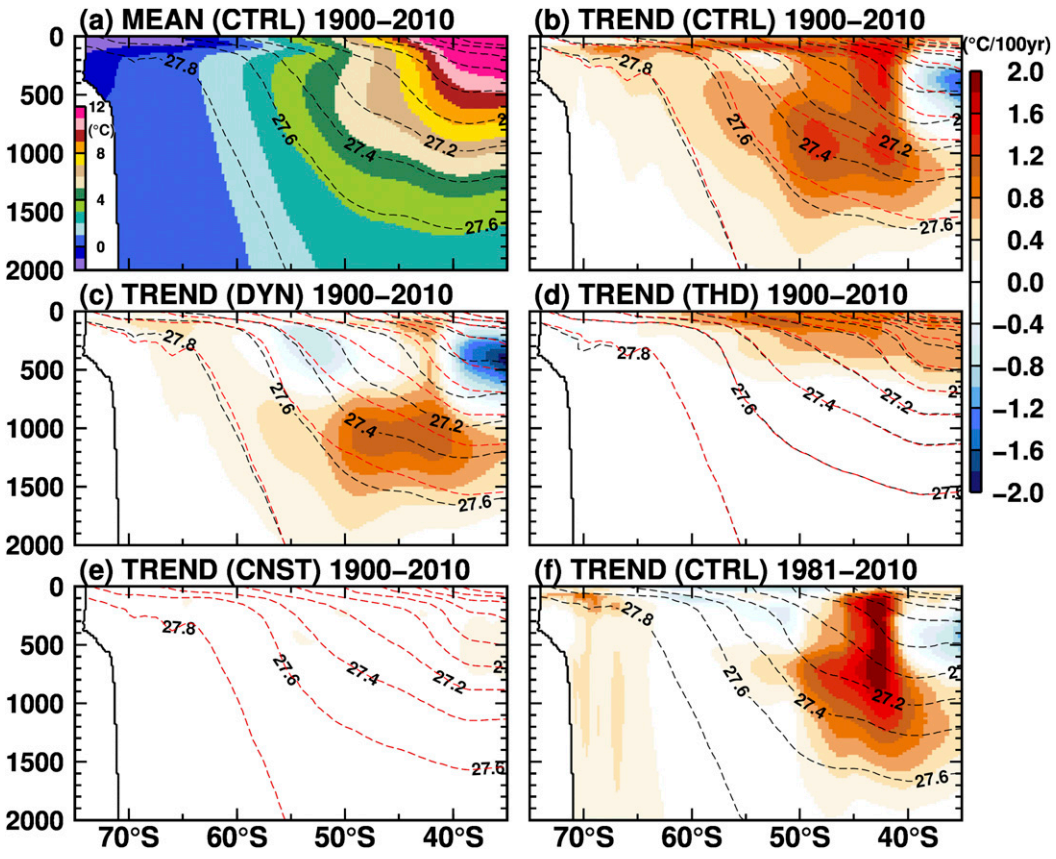

FIG. A7. (a) Vertical section of zonal mean annual temperature for the period 1900–2010 with contours of potential density. (b)–(e) Vertical sections of the linear trends in the zonal mean temperature for the period 1900–2010 in the CTRL, DYN, THD, and CNST cases. Red dashed contours in (b)–(e) are potential density in the CNST case. (f) Vertical section of the temperature trend for the period 1981–2010 in the CTRL case.

period 1981–2010 in the CTRL case, and the trend pattern is generally similar to that for the full period 1900–2010 (Fig. A7b). Note that a model study by Armour et al. (2016) demonstrated that warming signals over the Southern Ocean are explained by the convergence of an equatorward transport of anomalous heat gained south of the regions of the Antarctic Circumpolar Current. These results suggest that the ocean model captures the observed ocean temperature changes to some extent. Looking at the area south of 60°S, there is a local warming trend with a magnitude of up to 1.0°C century^{-1} in depths from 200 to 500 m (the layer between 27.6 and 27.8 kg m^{-3} of the potential density).

Changes in ocean circulation also contribute to heat flux variability. Here, we examine the mean and trend fields of the vertically integrated transport streamfunction (Fig. A8). Three large cyclonic wind-driven circulations are produced in the Weddell Sea, Australian–Antarctic Basin, and Ross Sea (Fig. A8a). For convenience, hereinafter we use the names Weddell Gyre, Kerguelen Gyre, and Ross Gyre for the three gyres (Gordon 2008). The mean magnitudes of the Weddell, Kerguelen, and Ross Gyres in the model for the period 1981–2010 are 33, 16, and 24 Sv (1 Sv $\equiv 10^6$ m^3 s^{-1}), respectively. Looking at the trend fields for the period 1900–2010 (Fig. A8b), the Weddell Gyre enhances the cyclonic circulation with a trend of 7.6 Sv century^{-1}, but the horizontal extent becomes smaller, shifting the eastern limb to the west. In the Kerguelen Gyre, there are negative trends along the coastal regions and positive trends in the center of the gyre, indicating flattening of the gyre against the coast. The Ross Gyre becomes stronger with a northward expansion at longitudes around 150°W with a trend of 4.7 Sv century^{-1}. The ACC transport measured in the Drake Passage in the CTRL case is 187 Sv, which is slightly larger than an observation-based estimate of 173 Sv (Donohue et al. 2016). The modeled ACC transport increases from below 170 Sv in the early twentieth century to about 185 Sv in the early twenty-first century.

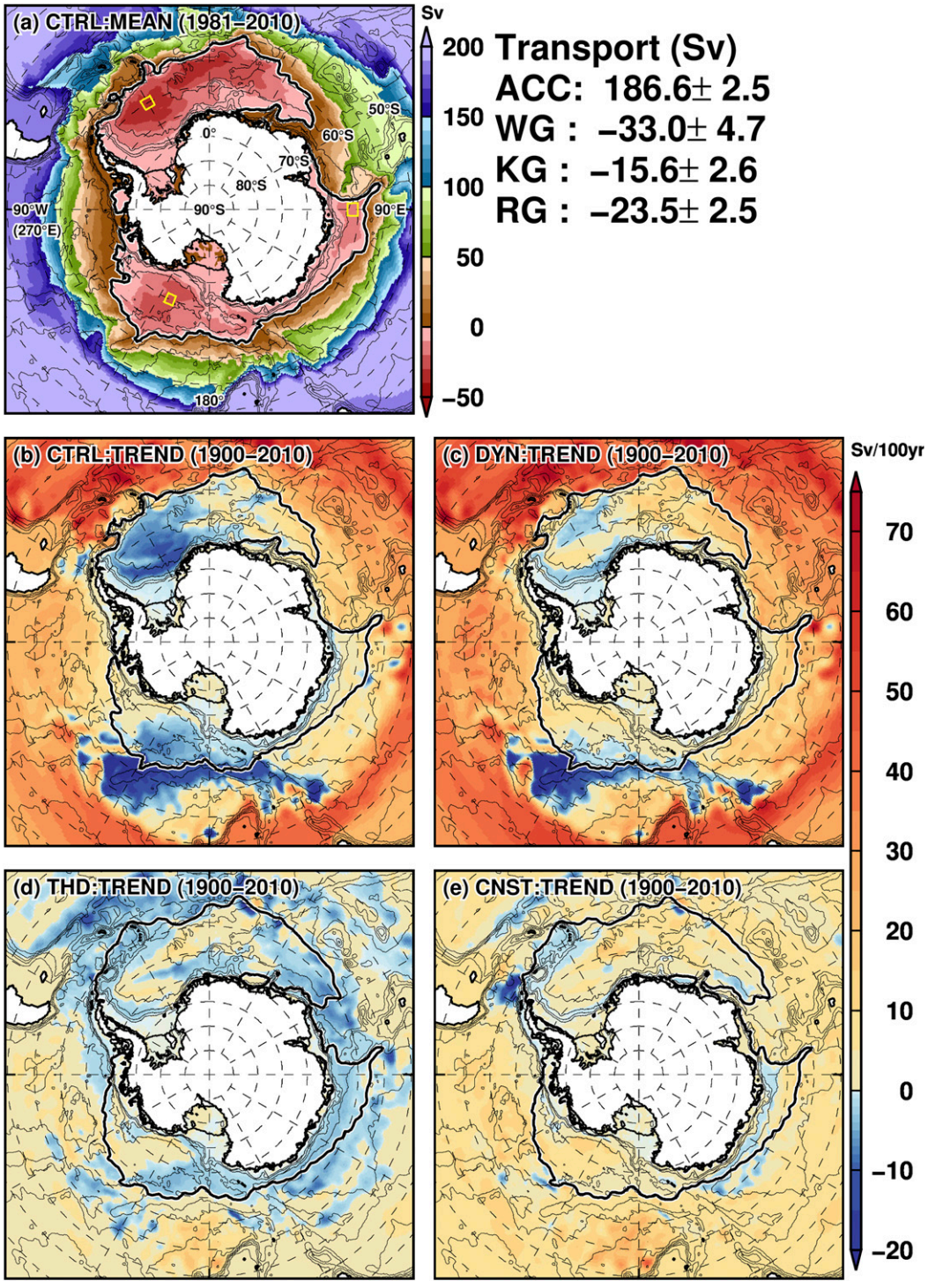

FIG. A8. Maps of vertically integrated transport streamfunctions: (a) mean and (b) linear trend in the CTRL case and (c)–(e) linear trends for the period 1900–2010 in the DYN, THD, and CNST cases. In (a) areas with negative values represent clockwise (cyclonic) circulation. In all panels, the thick black line indicates the zero line of the mean streamfunction in each case. The thin black lines show the depth contours at 1000-m intervals. The numbers next to (a) are mean volume transports (for the period 1981–2010) across the Drake Passage, and three large-scale cyclonic gyres. The yellow squares in (a) are the defined location of the gyres' centers.

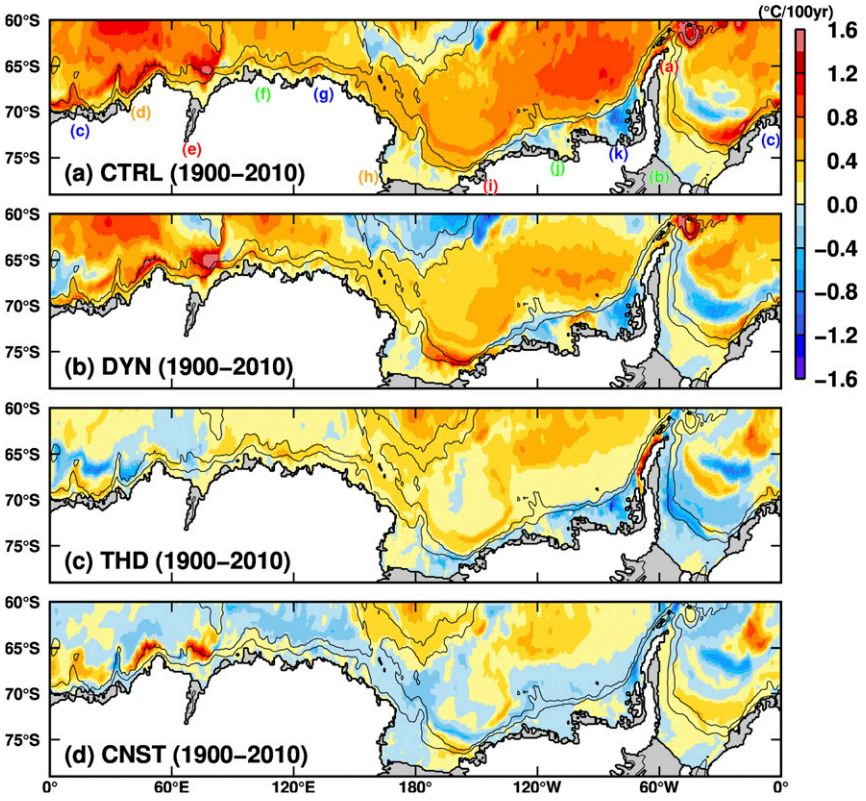

FIG. A9. Maps of linear trends in the subsurface temperature for the period 1900–2010 in the experiments: (a) CTRL case, (b) DYN case, (c) THD case, and (d) CNST case. The black contours show 1000- and 3000-m depth contours. In (a), labels of the ice shelf groups A–K are shown.

Along with the changes of the ocean gyres, there are pronounced basin-scale changes in the subsurface temperature, extending to the Antarctic coastal margins (Fig. A9; see also Fig. A7 for the zonal mean). Circumpolar warming trends are found on the shelf break/slope regions, with the largest warming trends in the Atlantic and Pacific sectors, where the coastward flows are enhanced (Fig. A8). It should be noted that there are regional cooling trends on the continental shelf regions in the Amundsen and Bellingshausen Seas, which are inconsistent with the observed warming trend in recent decades (Schmidtko et al. 2014). The model underestimates warm water intrusion from the continental shelf break/slope in these regions (Fig. 8). The deficiency of the warm water intrusion in the model results in the inconsistent regional basal melt trends (Fig. 7).

b. The responses of sea ice and ocean to dynamic and thermodynamic forcing

1) SEA ICE

Regarding Antarctic sea ice, we focus here on the total SIE and sea ice production. The total SIE is a good measure of the large-scale Antarctic sea ice–ocean response to atmospheric forcing, and sea ice production is the main driver for dense water formation along the Antarctic coastal margins. Figure A3b clearly demonstrates that while thermodynamic surface forcing is responsible for the winter maximum SIE trend, the combination of both dynamic and thermodynamic surface forcing controls the linear trend and interannual-to-decadal variability of the summer minimum SIE. These results are generally consistent with our previous sea ice modeling studies for the recent Antarctic sea ice trend (Kusahara et al. 2017a) and variability (Kusahara et al. 2019).

Next, we examine factors responsible for sea ice production (Fig. A5). Except for the Antarctic coastal margins, the large-scale distribution of sea ice production in the CTRL case is similar to that in the THD case, indicating that thermodynamic surface forcing (Fig. 2h) mainly controls sea ice formation and extent in offshore regions. On the other hand, the distribution of the coastal sea ice production in the CTRL case is quite similar to that in the DYN case (Figs. A5b,c). For example, the trend of the coastal sea ice production in the

Weddell Sea is almost explained by changes in dynamic forcing. Thermodynamic surface forcing partially accounts for the coastal sea ice production in the regions off the Wilkes Land, Ross Sea, and Amundsen-Bellingshausen Seas (Figs. A5b,d). The sea ice production in the CTRL case is roughly explained by the sum of those in the DYN and THD cases. Note that the trends in the three cases are different from the trend in the CNST case, which has a small and spatially unorganized trend (Fig. A5e). This assures that dynamic/thermodynamic surface forcing regulates the trend patterns in the experiments.

2) OCEAN

We now turn to separate contributions of dynamic and thermodynamic surface forcing on the trends in the zonal mean temperature (Fig. A7), the horizontal circulation (Fig. A8), and subsurface temperature (Fig. A9). A comparison of the temperature trends in the three experiments (Figs. A7b–d) demonstrates that dynamic and thermodynamic surface forcings have impacts on the temperature trend at different locations: wind stress regulates warming trends in intermediate depths from 500 to 1500 m at latitudes 60°–40°S, the subsurface cooling trend north of 40°S, and the subsurface warming trend at latitudes 70°–65°S, while thermodynamic forcing contributes to the subsurface warming trend at latitudes 60°–40°S. A comparison of density contours in the three cases with those in the CNST case allows us to examine the mechanism of the ocean temperature trends. The stronger winds (Fig. 2e) increase the tilt of the Southern Ocean isopycnals in the CTRL and DYN case, but there is no pronounced change in the THD and CNST cases. The isopycnal tilts lead to displacements of warm water in the intermediate depths at latitude 60°–40°S and subsurface in the coastal regions. The atmospheric warming effects (seen in Fig. A7d) are confined in the surface layers north of 60°S.

Looking at Figs. A8b–d, the large-scale ocean circulation trend is mainly controlled by wind stress changes (Fig. 2e), as can be inferred from wind-driven ocean circulation theory. The trend pattern in the THD case is discontinuous or patchy, and thus thermodynamic forcing is not a primary driver of large-scale ocean circulation but it modulates regional circulations. The trend pattern of the subsurface temperature in the CTRL case is similar to that in the DYN case in the coastal and shelf-break/slope regions and that in the THD case in the offshore regions (Fig. A8), which are consistent with the findings in the Fig. A7.

REFERENCES

Abram, N. J., E. R. Thomas, J. R. McConnell, R. Mulvaney, T. J. Bracegirdle, L. C. Sime, and A. J. Aristarain, 2010: Ice core evidence for a 20th century decline of sea ice in the Bellingshausen Sea, Antarctica. *J. Geophys. Res.*, **115**, D23101, https://doi.org/10.1029/2010JD014644.

——, R. Mulvaney, F. Vimeux, S. J. Phipps, J. Turner, and M. H. England, 2014: Evolution of the southern annular mode during the past millennium. *Nat. Climate Change*, **4**, 564–569, https://doi.org/10.1038/nclimate2235.

Adcroft, A., C. Hill, and J. Marshall, 1997: Representation of topography by shaved cells in a height coordinate ocean model. *Mon. Wea. Rev.*, **125**, 2293–2315, https://doi.org/10.1175/1520-0493(1997)125<2293:ROTBSC>2.0.CO;2.

Armour, K. C., J. Marshall, J. R. Scott, A. Donohoe, and E. R. Newsom, 2016: Southern Ocean warming delayed by circumpolar upwelling and equatorward transport. *Nat. Geosci.*, **9**, 549–554, https://doi.org/10.1038/ngeo2731.

Asay-Davis, X. S., N. C. Jourdain, and Y. Nakayama, 2017: Developments in simulating and parameterizing interactions between the Southern Ocean and the Antarctic ice sheet. *Curr. Climate Change Rep.*, **3**, 316–329, https://doi.org/10.1007/s40641-017-0071-0.

Beckmann, A., H. H. Hellmer, and R. Timmermann, 1999: A numerical model of the Weddell Sea: Large-scale circulation and water mass distribution. *J. Geophys. Res.*, **104**, 23 375–23 391, https://doi.org/10.1029/1999JC900194.

Bitz, C. M., and W. H. Lipscomb, 1999: An energy-conserving thermodynamic model of sea ice. *J. Geophys. Res.*, **104**, 15 669–15 677, https://doi.org/10.1029/1999JC900100.

Bracegirdle, T. J., and Coauthors, 2016: A multidisciplinary perspective on climate model evaluation for Antarctica. *Bull. Amer. Meteor. Soc.*, **97**, ES23–ES26, https://doi.org/10.1175/BAMS-D-15-00108.1.

——, and Coauthors, 2019: Back to the future: Using long-term observational and paleo-proxy reconstructions to improve model projections of Antarctic climate. *Geosciences*, **9**, 255, https://doi.org/10.3390/geosciences9060255.

Cavalieri, D. J., P. Gloersen, and W. J. Campbell, 1984: Determination of sea ice parameters with the Nimbus 7 SMMR. *J. Geophys. Res.*, **89**, 5355–5369, https://doi.org/10.1029/JD089iD04p05355.

——, C. L. Parkinson, and K. Y. Vinnikov, 2003: 30-year satellite record reveals contrasting Arctic and Antarctic decadal sea ice variability. *Geophys. Res. Lett.*, **30**, 1970, https://doi.org/10.1029/2003GL018031.

Chapman, W. L., and J. E. Walsh, 2007: A synthesis of Antarctic temperatures. *J. Climate*, **20**, 4096–4117, https://doi.org/10.1175/JCLI4236.1.

Comiso, J. C., R. Kwok, S. Martin, and A. L. Gordon, 2011: Variability and trends in sea ice extent and ice production in the Ross Sea. *J. Geophys. Res.*, **116**, C04021, https://doi.org/10.1029/2010JC006391.

——, R. A. Gersten, L. V. Stock, J. Turner, G. J. Perez, and K. Cho, 2017: Positive trend in the Antarctic sea ice cover and associated changes in surface temperature. *J. Climate*, **30**, 2251–2267, https://doi.org/10.1175/JCLI-D-16-0408.1.

Convey, P., and Coauthors, 2009: Antarctic climate change and the environment. *Antarct. Sci.*, **21**, 541–563, https://doi.org/10.1017/S0954102009990642.

Cook, A. J., A. J. Fox, D. G. Vaughan, and J. G. Ferrigno, 2005: Retreating glacier fronts on the Antarctic Peninsula over the past half-century. *Science*, **308**, 541–544, https://doi.org/10.1126/science.1104235.

——, P. R. Holland, M. P. Meredith, T. Murray, A. Luckman, and D. G. Vaughan, 2016: Ocean forcing of glacier retreat in the

western Antarctic Peninsula. *Science*, **353**, 283–286, https://doi.org/10.1126/science.aae0017.

Cotté, C., and C. Guinet, 2007: Historical whaling records reveal major regional retreat of Antarctic sea ice. *Deep-Sea Res. I*, **54**, 243–252, https://doi.org/10.1016/j.dsr.2006.11.001.

Curran, M. A. J., T. D. Van Ommen, V. I. Morgan, K. L. Phillips, and A. S. Palmer, 2003: Ice core evidence for Antarctic sea ice decline since the 1950s. *Science*, **302**, 1203–1206, https://doi.org/10.1126/science.1087888.

de la Mare, W. K., 1997: Abrupt mid-twentieth-century decline in Antarctic sea-ice extent from whaling records. *Nature*, **389**, 57–60, https://doi.org/10.1038/37956.

Depoorter, M. A., J. L. Bamber, J. A. Griggs, J. T. M. Lenaerts, S. R. M. Ligtenberg, M. R. van den Broeke, and G. Moholdt, 2013: Calving fluxes and basal melt rates of Antarctic ice shelves. *Nature*, **502**, 89–92, https://doi.org/10.1038/nature12567.

De Santis, A., E. Maier, R. Gomez, and I. Gonzalez, 2017: Antarctica, 1979–2016 sea ice extent: Total versus regional trends, anomalies, and correlation with climatological variables. *Int. J. Remote Sens.*, **38**, 7566–7584, https://doi.org/10.1080/01431161.2017.1363440.

Dinniman, M., X. Asay-Davis, B. Galton-Fenzi, P. Holland, A. Jenkins, and R. Timmermann, 2016: Modeling ice shelf/ocean interaction in Antarctica: A review. *Oceanography*, **29**, 144–153, https://doi.org/10.5670/oceanog.2016.106.

Donohue, K. A., K. L. Tracey, D. R. Watts, M. P. Chidichimo, and T. K. Chereskin, 2016: Mean Antarctic Circumpolar Current transport measured in Drake Passage. *Geophys. Res. Lett.*, **43**, 11 760–11 767, https://doi.org/10.1002/2016GL070319.

Downes, S. M., and Coauthors, 2015: An assessment of Southern Ocean water masses and sea ice during 1988–2007 in a suite of interannual CORE-II simulations. *Ocean Modell.*, **94**, 67–94, https://doi.org/10.1016/j.ocemod.2015.07.022.

Fan, T., C. Deser, and D. P. Schneider, 2014: Recent Antarctic sea ice trends in the context of Southern Ocean surface climate variations since 1950. *Geophys. Res. Lett.*, **41**, 2419–2426, https://doi.org/10.1002/2014GL059239.

Flato, G., and Coauthors, 2013: Evaluation of climate models. *Climate Change 2013: The Physical Science Basis*, T. F. Stocker et al., Eds., Cambridge University Press, 741–866.

Fogt, R. L., J. Perlwitz, A. J. Monaghan, D. H. Bromwich, J. M. Jones, and G. J. Marshall, 2009: Historical SAM variability. Part II: Twentieth-century variability and trends from reconstructions, Observations, and the IPCC AR4 models. *J. Climate*, **22**, 5346–5365, https://doi.org/10.1175/2009JCLI2786.1.

Fraser, A. D., R. A. Massom, K. J. Michael, B. K. Galton-Fenzi, and J. L. Lieser, 2012: East Antarctic landfast sea ice distribution and variability, 2000–08. *J. Climate*, **25**, 1137–1156, https://doi.org/10.1175/JCLI-D-10-05032.1.

Gagné, M., N. P. Gillett, and J. C. Fyfe, 2015: Observed and simulated changes in Antarctic sea ice extent over the past 50 years. *Geophys. Res. Lett.*, **42**, 90–95, https://doi.org/10.1002/2014GL062231.

Gent, P. R., J. Willebrand, T. J. McDougall, and J. C. McWilliams, 1995: Parameterizing eddy-induced tracer transports in ocean circulation models. *J. Phys. Oceanogr.*, **25**, 463–474, https://doi.org/10.1175/1520-0485(1995)025<0463:PEITTI>2.0.CO;2.

Gille, S. T., 2002: Warming of the Southern Ocean since the 1950s. *Science*, **295**, 1275–1277, https://doi.org/10.1126/science.1065863.

Gong, D., and S. Wang, 1999: Definition of Antarctic oscillation index. *Geophys. Res. Lett.*, **26**, 459–462, https://doi.org/10.1029/1999GL900003.

Goosse, H., W. Lefebvre, A. de Montety, E. Crespin, and A. H. Orsi, 2009: Consistent past half-century trends in the atmosphere, the sea ice and the ocean at high southern latitudes. *Climate Dyn.*, **33**, 999–1016 https://doi.org/10.1007/s00382-008-0500-9.

Gordon, A. L., 2008: Current systems in the Southern Ocean. *Encyclopedia of Ocean Sciences*, 2nd ed., Academic Press, 735–743, https://doi.org/10.1016/B978-012374473-9.00369-6.

Gwyther, D. E., K. Kusahara, X. S. Asay-Davis, M. S. Dinniman, and B. K. Galton-Fenzi, 2020: Vertical processes and resolution impact ice shelf basal melting: A multi-model study. *Ocean Modell.*, **147**, 101569, https://doi.org/10.1016/J.OCEMOD.2020.101569.

Hellmer, H. H., 2004: Impact of Antarctic ice shelf basal melting on sea ice and deep ocean properties. *Geophys. Res. Lett.*, **31**, L10307, https://doi.org/10.1029/2004GL019506.

——, and D. J. Olbers, 1989: A two-dimensional model for the thermohaline circulation under an ice shelf. *Antarct. Sci.*, **1**, 325–336, https://doi.org/10.1017/S0954102089000490.

——, F. Kauker, R. Timmermann, J. Determann, and J. Rae, 2012: Twenty-first-century warming of a large Antarctic ice-shelf cavity by a redirected coastal current. *Nature*, **485**, 225–228, https://doi.org/10.1038/nature11064.

Hibler, W. D., 1979: A dynamic thermodynamic sea ice model. *J. Phys. Oceanogr.*, **9**, 815–846, https://doi.org/10.1175/1520-0485(1979)009<0815:ADTSIM>2.0.CO;2.

Hobbs, W., M. Curran, N. Abram, and E. R. Thomas, 2016a: Century-scale perspectives on observed and simulated Southern Ocean sea ice trends from proxy reconstructions. *J. Geophys. Res. Oceans*, **121**, 7804–7818, https://doi.org/10.1002/2016JC012111.

——, R. Massom, S. Stammerjohn, P. Reid, G. Williams, and W. Meier, 2016b: A review of recent changes in Southern Ocean sea ice, their drivers and forcings. *Global Planet. Change*, **143**, 228–250, https://doi.org/10.1016/j.gloplacha.2016.06.008.

Holland, D. M., and A. Jenkins, 1999: Modeling thermodynamic ice–ocean interactions at the base of an ice shelf. *J. Phys. Oceanogr.*, **29**, 1787–1800, https://doi.org/10.1175/1520-0485(1999)029<1787:MTIOIA>2.0.CO;2.

Holland, P. R., 2014: The seasonality of Antarctic sea ice trends. *Geophys. Res. Lett.*, **41**, 4230–4237, https://doi.org/10.1002/2014GL060172.

Hunke, E. C., and J. K. Dukowicz, 1997: An elastic-viscous-plastic model for sea ice dynamics. *J. Phys. Oceanogr.*, **27**, 1849–1867, https://doi.org/10.1175/1520-0485(1997)027<1849:AEVPMF>2.0.CO;2.

Jacobs, S. S., and C. F. Giulivi, 2010: Large multidecadal salinity trends near the Pacific–Antarctic continental margin. *J. Climate*, **23**, 4508–4524, https://doi.org/10.1175/2010JCLI3284.1.

——, H. H. Hellmer, C. S. M. Doake, A. Jenkins, and R. M. Frolich, 1992: Melting of ice shelves and the mass balance of Antarctica. *J. Glaciol.*, **38**, 375–387, https://doi.org/10.1017/S0022143000002252.

Jones, J. M., and Coauthors, 2016: Assessing recent trends in high-latitude Southern Hemisphere surface climate. *Nat. Climate Change*, **6**, 917–926, https://doi.org/10.1038/nclimate3103.

Kara, A. B., P. A. Rochford, and H. E. Hurlburt, 2000: Efficient and accurate bulk parameterizations of air–sea fluxes for use in general circulation models. *J. Atmos. Oceanic Technol.*, **17**, 1421–1438, https://doi.org/10.1175/1520-0426(2000)017<1421:EAABPO>2.0.CO;2.

Kusahara, K., and H. Hasumi, 2013: Modeling Antarctic ice shelf responses to future climate changes and impacts on the ocean. *J. Geophys. Res. Oceans*, **118**, 2454–2475, https://doi.org/10.1002/jgrc.20166.

——, and ——, 2014: Pathways of basal meltwater from Antarctic ice shelves: A model study. *J. Geophys. Res. Oceans*, **119**, 5690–5704, https://doi.org/10.1002/2014JC009915.

——, ——, and T. Tamura, 2010: Modeling sea ice production and dense shelf water formation in coastal polynyas around East Antarctica. *J. Geophys. Res.*, **115**, C10006, https://doi.org/10.1029/2010JC006133.

——, G. D. Williams, R. Massom, P. Reid, and H. Hasumi, 2017a: Roles of wind stress and thermodynamic forcing in recent trends in Antarctic sea ice and Southern Ocean SST: An ocean–sea ice model study. *Global Planet. Change*, **158**, 103–118, https://doi.org/10.1016/j.gloplacha.2017.09.012.

——, ——, T. Tamura, R. Massom, and H. Hasumi, 2017b: Dense Shelf Water spreading from Antarctic coastal polynyas to the deep Southern Ocean: A regional circumpolar model study. *J. Geophys. Res. Ocean*, **122**, 6238–6253, https://doi.org/10.1002/2017JC012911.

——, ——, R. Massom, P. Reid, and H. Hasumi, 2019: Spatiotemporal dependence of Antarctic sea ice variability to dynamic and thermodynamic forcing: A coupled ocean–sea ice model study. *Climate Dyn.*, **52**, 3791–3807, https://doi.org/10.1007/s00382-018-4348-3.

Marshall, G. J., 2003: Trends in the southern annular mode from observations and reanalyses. *J. Climate*, **16**, 4134–4143, https://doi.org/10.1175/1520-0442(2003)016<4134:TITSAM>2.0.CO;2.

Massom, R., P. T. Harris, K. J. Michael, and M. J. Potter, 1998: The distribution and formative processes of latent-heat polynyas in East Antarctica. *Ann. Glaciol.*, **27**, 420–426, https://doi.org/10.3189/1998AoG27-1-420-426.

——, P. Reid, S. Stammerjohn, B. Raymond, A. Fraser, and S. Ushio, 2013: Change and variability in East Antarctic sea ice seasonality, 1979/80–2009/10. *PLOS ONE*, **8**, e64756, https://doi.org/10.1371/journal.pone.0064756.

Mathiot, P., A. Jenkins, C. Harris, and G. Madec, 2017: Explicit representation and parametrised impacts of under ice shelf seas in the z^* coordinate ocean model NEMO 3.6. *Geosci. Model Dev.*, **10**, 2849–2874, https://doi.org/10.5194/gmd-10-2849-2017.

Meier, W. N., D. Gallaher, and G. G. Campbell, 2013: New estimates of Arctic and Antarctic sea ice extent during September 1964 from recovered Nimbus I satellite imagery. *Cryosphere*, **7**, 699–705, https://doi.org/10.5194/tc-7-699-2013.

Mellor, G. L., and L. Kantha, 1989: An ice–ocean coupled model. *J. Geophys. Res.*, **94**, 10 937–10 954, https://doi.org/10.1029/JC094iC08p10937.

Morales Maqueda, M. A., A. J. Willmott, and N. R. T. Biggs, 2004: Polynya dynamics: A review of observations and modeling. *Rev. Geophys.*, **42**, RG1004, https://doi.org/10.1029/2002RG000116.

Murphy, E. J., A. Clarke, N. J. Abram, and J. Turner, 2014: Variability of sea-ice in the northern Weddell Sea during the 20th century. *J. Geophys. Res. Ocean*, **119**, 4549–4572, https://doi.org/10.1002/2013JC009511.

Nakayama, Y., R. Timmermann, M. Schröder, and H. H. Hellmer, 2014: On the difficulty of modeling Circumpolar Deep Water intrusions onto the Amundsen Sea continental shelf. *Ocean Modell.*, **84**, 26–34, https://doi.org/10.1016/j.ocemod.2014.09.007.

Naughten, K. A., K. J. Meissner, B. K. Galton-Fenzi, M. H. England, R. Timmermann, and H. H. Hellmer, 2018: Future projections of Antarctic ice shelf melting based on CMIP5 scenarios. *J. Climate*, **31**, 5243–5261, https://doi.org/10.1175/JCLI-D-17-0854.1.

Nihashi, S., and K. I. Ohshima, 2015: Circumpolar mapping of Antarctic coastal polynyas and landfast sea ice: Relationship and variability. *J. Climate*, **28**, 3650–3670, https://doi.org/10.1175/JCLI-D-14-00369.1.

Noh, Y., and H. J. Kim, 1999: Simulations of temperature and turbulence structure of the oceanic boundary layer with the improved near-surface process. *J. Geophys. Res.*, **104**, 15 621–15 634, https://doi.org/10.1029/1999JC900068.

Obase, T., A. Abe-Ouchi, K. Kusahara, H. Hasumi, and R. Ohgaito, 2017: Responses of basal melting of Antarctic ice shelves to the climatic forcing of the Last Glacial Maximum and CO_2 doubling. *J. Climate*, **30**, 3473–3497, https://doi.org/10.1175/JCLI-D-15-0908.1.

Paolo, F. S., H. A. Fricker, and L. Padman, 2015: Volume loss from Antarctic ice shelves is accelerating. *Science*, **348**, 327–331, https://doi.org/10.1126/science.aaa0940.

Parkinson, C. L., 2019: A 40-y record reveals gradual Antarctic sea ice increases followed by decreases at rates far exceeding the rates seen in the Arctic. *Proc. Natl. Acad. Sci. USA*, **116**, 14414–14423, https://doi.org/10.1073/pnas.1906556116.

——, and D. J. Cavalieri, 2012: Antarctic sea ice variability and trends, 1979–2010. *Cryosphere*, **6**, 871–880, https://doi.org/10.5194/tc-6-871-2012.

Poli, P., and Coauthors, 2016: ERA-20C: An atmospheric reanalysis of the twentieth century. *J. Climate*, **29**, 4083–4097, https://doi.org/10.1175/JCLI-D-15-0556.1.

Pritchard, H. D., S. R. M. Ligtenberg, H. A. Fricker, D. G. Vaughan, M. R. van den Broeke, and L. Padman, 2012: Antarctic ice-sheet loss driven by basal melting of ice shelves. *Nature*, **484**, 502–505, https://doi.org/10.1038/nature10968.

Purkey, S. G., and G. C. Johnson, 2010: Warming of global abyssal and deep Southern Ocean waters between the 1990s and 2000s: Contributions to global heat and sea level rise budgets. *J. Climate*, **23**, 6336–6351, https://doi.org/10.1175/2010JCLI3682.1.

Rayner, N. A., D. E. Parker, E. B. Horton, C. K. Folland, L. V. Alexander, D. P. Rowell, E. C. Kent, and A. Kaplan, 2003: Global analyses of sea surface temperature, sea ice, and night marine air temperature since the late nineteenth century. *J. Geophys. Res.*, **108**, 4407, https://doi.org/10.1029/2002JD002670.

Rignot, E., J. L. Bamber, M. R. van den Broeke, C. Davis, Y. Li, W. J. van de Berg, and E. van Meijgaard, 2008: Recent Antarctic ice mass loss from radar interferometry and regional climate modelling. *Nat. Geosci.*, **1**, 106–110, https://doi.org/10.1038/ngeo102.

——, I. Velicogna, M. R. van den Broeke, A. Monaghan, and J. Lenaerts, 2011: Acceleration of the contribution of the Greenland and Antarctic ice sheets to sea level. *Geophys. Res. Lett.*, **38**, L05503, https://doi.org/10.1029/2011GL046583.

——, S. Jacobs, J. Mouginot, and B. Scheuchl, 2013: Ice-shelf melting around Antarctica. *Science*, **341**, 266–270, https://doi.org/10.1126/science.1235798.

Sallée, J.-B., 2018: Southern Ocean warming. *Oceanography*, **31**, 52–62, https://doi.org/10.5670/oceanog.2018.215.

Schaffer, J., R. Timmermann, J. Erik Arndt, S. Savstrup Kristensen, C. Mayer, M. Morlighem, and D. Steinhage, 2016: A global, high-resolution data set of ice sheet topography, cavity geometry, and ocean bathymetry. *Earth Syst. Sci. Data*, **8**, 543–557, https://doi.org/10.5194/essd-8-543-2016.

Schmidtko, S., K. J. Heywood, A. F. Thompson, and S. Aoki, 2014: Multidecadal warming of Antarctic waters. *Science*, **346**, 1227–1231, https://doi.org/10.1126/science.1256117.

Schodlok, M. P., D. Menemenlis, and E. J. Rignot, 2016: Ice shelf basal melt rates around Antarctica from simulations and

observations. *J. Geophys. Res. Ocean*, **121**, 1085–1109, https://doi.org/10.1002/2015JC011117.

Shepherd, A., D. Wingham, D. Wallis, K. Giles, S. Laxon, and A. V. Sundal, 2010: Recent loss of floating ice and the consequent sea level contribution. *Geophys. Res. Lett.*, **37**, L13503, https://doi.org/10.1029/2010GL042496.

Stammerjohn, S., D. G. Martinson, R. C. Smith, X. Yuan, and D. Rind, 2008: Trends in Antarctic annual sea ice retreat and advance and their relation to El Niño–Southern Oscillation and southern annular mode variability. *J. Geophys. Res.*, **113**, C03S90, https://doi.org/10.1029/2007JC004269.

——, R. Massom, D. Rind, and D. Martinson, 2012: Regions of rapid sea ice change: An inter-hemispheric seasonal comparison. *Geophys. Res. Lett.*, **39**, L06501, https://doi.org/10.1029/2012GL050874.

Steele, M., M. Steele, R. Morley, R. Morley, W. Ermold, and W. Ermold, 2001: PHC: A global ocean hydrography with a high-quality Arctic Ocean. *J. Climate*, **14**, 2079–2087, https://doi.org/10.1175/1520-0442(2001)014<2079:PAGOHW>2.0.CO;2.

Swart, N. C., S. T. Gille, J. C. Fyfe, and N. P. Gillett, 2018: Recent Southern Ocean warming and freshening driven by greenhouse gas emissions and ozone depletion. *Nat. Geosci.*, **11**, 836–841, https://doi.org/10.1038/s41561-018-0226-1.

Swift, C. T., and D. J. Cavalieri, 1985: Passive microwave remote sensing for sea ice research. *Eos, Trans. Amer. Geophys. Union*, **66**, 1210–1212, https://doi.org/10.1029/EO066i049p01210.

Tamura, T., K. I. Ohshima, and S. Nihashi, 2008: Mapping of sea ice production for Antarctic coastal polynyas. *Geophys. Res. Lett.*, **35**, L07606, https://doi.org/10.1029/2007GL032903.

Thompson, D. W. J., and J. M. Wallace, 2000: Annular modes in the extratropical circulation. Part II: Trends. *J. Climate*, **13**, 1018–1036, https://doi.org/10.1175/1520-0442(2000)013<1018:AMITEC>2.0.CO;2.

Timmermann, R., and H. H. Hellmer, 2013: Southern Ocean warming and increased ice shelf basal melting in the twenty-first and twenty-second centuries based on coupled ice-ocean finite-element modelling. *Ocean Dyn.*, **63**, 1011–1026, https://doi.org/10.1007/s10236-013-0642-0.

——, and Coauthors, 2010: A consistent dataset of Antarctic ice sheet topography, cavity geometry, and global bathymetry. *Earth Syst. Sci. Data Discuss.*, **3**, 231–257, https://doi.org/10.5194/essdd-3-231-2010.

——, Q. Wang, and H. H. Hellmer, 2012: Ice-shelf basal melting in a global finite-element sea-ice/ice-shelf/ocean model. *Ann. Glaciol.*, **53**, 303–314, https://doi.org/10.3189/2012AoG60A156.

Turner, J., and Coauthors, 2004: The SCAR READER project: Toward a high-quality database of mean Antarctic meteorological observations. *J. Climate*, **17**, 2890–2898, https://doi.org/10.1175/1520-0442(2004)017<2890:TSRPTA>2.0.CO;2.

——, and Coauthors, 2009: *Antarctic Climate Change and the Environment*. Scientific Committee for Antarctic Research, 526 pp.

——, and Coauthors, 2014: Antarctic climate change and the environment: An update. *Polar Rec.*, **50**, 237–259, https://doi.org/10.1017/S0032247413000296.

——, G. J. Marshall, K. Clem, S. Colwell, T. Phillips, and H. Lu, 2019: Antarctic temperature variability and change from station data. *Int. J. Climatol.*, https://doi.org/10.1002/JOC.6378.